2019•2020

Faculteit Industriële ingenieurswetenschappen

master in de industriële wetenschappen: nucleaire technologie

Masterthesis

Design and manufacturing of a thoracic phantom using 3D-printing and bone equivalent material

PROMOTOR :

Prof. dr. Brigitte RENIERS

Jarne Withouck

Scriptie ingediend tot het behalen van de graad van master in de industriële wetenschappen: nucleaire technologie, afstudeerrichting nucleaire technieken / medisch nucleaire technieken

Gezamenlijke opleiding UHasselt en KU Leuven

UHASSELT

KU LEUVEN

UHASSELT

KU LEUVEN

2019•2020

Faculteit Industriële ingenieurswetenschappen

master in de industriële wetenschappen: nucleaire technologie

Masterthesis

Design and manufacturing of a thoracic phantom using 3D-printing and bone equivalent material

PROMOTOR :

Prof. dr. Brigitte RENIERS

Jarne Withouck

Scriptie ingediend tot het behalen van de graad van master in de industriële wetenschappen: nucleaire technologie, afstudeerrichting nucleaire technieken / medisch nucleaire technieken

UHASSELT KU LEUVEN

Preface

The creation of this Master's thesis was not a small feat, It took up a serious amount of time combining all knowledge I gathered throughout my studies. I would like to thank several people and institutions that made the creation of this Master's thesis possible. Not every single person is mentioned by name but all of them I want to thank immensely for all their help and support.

First I would like to thank my supervisor, prof. dr. Brigitte Reniers for the aid in helping me find a subject which was both interesting and especially useful in further development of medical dosimetry in radiotherapy. She gave me the opportunity to combine the learning of different aspects of 3D-printing with medical dosimetry. She was always available to answer questions if they happened to present themselves and supported me in this period while keeping confidence in me and the study.

A thanks also goes out to the Hasselt University (UHasselt) and the Nuclear Technological Centre (NuTeC), all located in Diepenbeek, Belgium for giving me the opportunity to conduct this research while using their equipment. The Makerspace and their employees deserve a special thanks since they assisted me in every part of the 3D-printing process, without their knowledge and tips the 3D-printing would have taken a much longer time.

A special thanks goes out to the Jessa hospital in Hasselt and the Maastro clinic in Maastricht. I was always welcomed warmly with them always providing time and assistance when needed/possible even with their busy schedules.

Furthermore, I would like to express my thanks to all those who supported me through all the years of being a student, especially my parents for presenting me with the chances and possibilities. They kept supporting me through every difficult period and kept believing in me. Next I want to thank my friends and fellow students for always being there when necessary. Their unconditional support throughout this entire period was a giant and well received help.

Table of contents

List of tables

List of figures

Abstract

In radiation therapy it is desired to deliver a high radiation dose to a target volume while keeping the toxicities to healthy tissue low. To ensure that the planned and delivered dose distributions are as equal as possible, the use of dosimetry phantoms in radiation therapy is critical.

This Master's thesis aimed to investigate the possibility to fabricate a thoracic phantom containing bone equivalent material using a cost-effective 3D-printing technique with equivalent imaging and dosimetry properties for radiotherapy by comparing calculated (AXB_M) and measured dose distributions. A phantom containing lungs and soft tissue was first designed using 3D-software after which it was printed, using varying infill densities, and assembled. Bone equivalent material was investigated using two types of RTV-silicone mixed with various amounts of $CaCO_3$.

Good agreements for the imaging properties were obtained for all structures. However, results for dosimetry in two clinics using EBT3 film dosimetry were representable only when using one-scan dosimetry, showing a max deviation of 4.1 % at heterogenous areas containing bone. L-α-alanine dosimetry presented a max underestimation of the TPS of 3.2 % in clinic 1 and 3.1 % in clinic 2. Further adaptations to the phantom are necessary, especially for the production of higher density bone equivalent material.

Abstract (Nederlandstalig)

Bij radiotherapie is het gewenst om een hoge stralingsdosis aan een doelvolume af te geven terwijl de toxiciteit voor gezond weefsel laag blijft. Om ervoor te zorgen dat de geplande en afgegeven dosisverdelingen zo gelijk mogelijk zijn, is het gebruik van fantomen voor dosimetrie in radiotherapie van cruciaal belang.

Deze masterproef had als doel het onderzoeken van de mogelijkheid om een thoracaal fantoom dat botequivalent materiaal bevat te fabriceren met behulp van een kosteneffectieve 3D-printtechniek. Het fantoom moet correcte eigenschappen voor beeldvorming en radiotherapeutische dosimetrie vertonen door berekende (AXB_M) en gemeten dosisverdelingen te vergelijken. Een fantoom met longen en zacht weefsel werd ontworpen met behulp van 3D-software, waarna het met verschillende opvul-dichtheden werd geprint en geassembleerd. Bot equivalent materiaal werd onderzocht met behulp van twee soorten RTV-siliconen gemengd met verscheidene hoeveelheden $CaCO_3$.

De beeldvormingseigenschappen waren equivalent met menselijk weefsel bij alle structuren. De resultaten voor EBT3-filmdosimetrie in twee ziekenhuizen waren enkel representatief bij gebruik van de one-scan methode, met een max afwijking van 4.1 % bij heterogene gebieden die bot bevatten. L-α-alanine dosimetrie vertoonde een max onderschatting van het TPS van 3,2 % in kliniek 1 en 3,1 % in kliniek 2. Verdere aanpassingen aan het fantoom zijn noodzakelijk, vooral voor de productie van bot equivalent materiaal met hogere dichtheid.

1 Introduction

Malignant (cancerous) and certain benign diseases being treated using ionizing radiation is the concept of radiation therapy. The goal is to deliver the highest possible radiation dose to a tumor or target volume while keeping the toxicities to normal, healthy tissue as low as possible. It is necessary to maximize the ratio between the tumor control probability (TCP) and the healthy tissue complications probability, known as the therapeutic ratio [1], [2].
In ensuring safe and effective treatment for patients, thus having an as equal as possible planned and delivered dose distribution, dosimetry phantoms play an important role. The spatial distribution of absolute dose throughout the human body of a patient is an extremely important factor for the successful use of external beam radiation therapy (EBRT) for therapeutic use. Phantoms can control calibration and characterization of delivery devices and they offer a verification method for the planned and calculated dose distributions of the treatment plans [3], [4].

Dose calculation algorithms are utilized for the evaluation of dose distribution throughout these phantoms or real patient bodies of which AcurosXB (Varian Medical Systems) is the latest addition. These algorithms should consequently proof capable of calculating dose distributions throughout heterogenous volumes. The thorax is an example of such a volume. It contains, among other tissue, soft tissue, lung tissue and bone tissue [5].
When the ideal materials to obtain the best possible representation of the human body are investigated for use in dosimetry phantoms, it is often associated with high costs. Typically three sorts of tissue equivalent materials are used in phantoms that are commercially available. These are materials that mimic soft tissue, lung and bone. High quality phantoms that are used primarily for diagnostic imaging studies have a limitation, which is their prohibitive costs ranging upwards of 16 000 euro [6]

Three-dimensional (3D) printing with the use of fused deposition modeling (FDM) technology has been used to manufacture anthropomorphic phantoms for measurements of radiation therapy dose. These can then be produced cost-effectively using polymers including polyurethane, polylactic acid (PLA) and epoxy resins. [7], [8].
It is often difficult and complicated to adopt the production methods of these 3D-printed phantoms for clinical use. Equivalency to imaging properties of human tissue is achievable by most of these phantoms. However, equivalency of radiation attenuation to the represented tissue has in many cases not been proven. Since the applications in clinic of various anthropomorphic phantoms include dose verification, quality assurance (QA), equipment calibration and more, they should be designed containing attenuation characteristics and anatomy similar to human tissue [9], [10].

In this Master's thesis the ideal settings to design, and materials to manufacture a 3D-printed thoracic phantom containing tissue equivalent materials for soft tissue, lung and bone are investigated. The resulting phantom should have properties acceptable for both imaging and dosimetry whilst keeping the cost low. To achieve this an alternative for bone equivalent material is investigated by using different types of room temperature vulcanizing (RTV) silicone. Various amounts of calcium carbonate ($CaCO_3$) are added to achieve similar imaging properties and corresponding densities compared to bone tissue. The mixture was subsequently poured in 3D-printed molds of the spine and ribs using PLA and left to cure for at least one hour.

To validate the manufactured phantom in its entirety, the dose plan calculated by AcurosXB dose to medium (AXB_M) had to be compared to the absorbed dose measured at several places throughout the 3D-printed thoracic phantom. Absorbed dose can be measured by a number of methods and dosimeters. Using a combination of L-alanine and EBT3 gafchromic films should provide a reliable verification method to compare the absorbed dose calculated by AXB_M to the measured absorbed dose.

2 Literature study

2.1 Radiation therapy

Malignant (cancerous) and certain benign diseases being treated using ionizing radiation is the concept of radiation therapy. During the treatment of cancer, the irradiation of tumor cells is performed with the use of ionizing radiation such as X-rays. This type of irradiation causes damage to the DNA due to the direct and indirect process of free radical production which ultimately can lead to cell death. However this is also true for surrounding healthy cells. Healthy cells usually depict a faster repair rate than cancerous cells while retaining their normal function status. The difference in repair efficiency results in differential cancer cell killing [1], [2].

Consequently, Delivering the highest possible radiation dose to a tumor while keeping the toxicities to normal tissue as low as possible is the goal of radiotherapy. It can be generally stated that conformal dose distributions, patient immobilization, precise alignment and motion management are requirements in attaining the goal to give the highest dose to the target volume while sparing the healthy surrounding tissue [1].

2.1.1 Treatment possibilities

Two ways of delivering radiation to the cancer location exist, which are EBRT and brachytherapy. EBRT delivers radiation to the target by aiming high energy photons, protons or particle radiation from outside the body. In the clinical setting this is the most common approach. For brachytherapy the radiation is delivered internally by radioactive sources sealed in catheters or by seeds planted in the tumor site itself [2].

2.1.1.1 3D Conformal radiotherapy (3DCRT)

2D radiation therapy based on normal X-ray imaging utilizing rectangular fields has found its replacement in 3D radiation therapy based on CT imaging. This allows the localization of the tumor in a more accurate way and aids in optimal shielding and beam placement. The goal is to deliver the radiation to the gross tumor volume (GTV). Around the GTV there is a margin for a microscopic extension of the tumor which is called the clinical target volume (CTV). Around the CTV another margin exists to take into account the uncertainties concerning setup variations and organ motion which is called the planning target volume (PTV) [2].

2.1.1.2 Intensity modulated radiation therapy (IMRT)

Radiation doses conforming to the tumor whilst avoiding critical organs by creating irregular-shaped dose distribution can be achieved with IMRT. Intensity-modulation, that is computer controlled, during treatment of multiple radiation beams and inverse planning software makes IMRT possible. The multiple radiation beams are dynamically collimated at certain static angles resulting in a highly conformal three-dimensional distribution of the dose. A multi-leaf collimator is usually utilized to deliver five to seven fields with irregular fluence patterns. Inverse planning is performed by starting with the specifications of the dose constraints after which the computer software optimizes a fluence map. The resulting fluence map is then achieved by positioning the MLC leafs automatically. Many clinical departments offer IMRT which can be delivered by linear accelerators. It is available for both static or dynamic multi-leaf collimators and tomotherapy machines. [1] [2].

2.1.1.3 Volumetric modulated arc therapy (VMAT)

VMAT forms a complete arc around the target structure by utilizing a non-stop modulated delivery of radiation with gantry rotation. A conformal delivery equivalent or even superior to IMRT can be provided by VMAT due to the dose rate, variable multileaf collimator (MLC) leaf position and the gantry speed. Furthermore the treatment time is decreased as are the monitor units (MU). In order to optimize all variables it is also necessary to use inverse planning for this technique [1].

2.1.1.4 Image-guided radiation therapy (IGRT)

Patient setup variations and organ motion combined with treatment margins becoming more conformal and tighter, the potential risk to miss the tumor becomes greater. A slight positional error due to critical structures being close to the tumor may also lead to radiation of normal tissues and organs which is not desired. These errors can be detected by IGRT thanks to information from pre-therapy imaging and be adjusted for by position correction. An example for this is the usage of daily cone-beam computed tomography (CBCT) scans acquired before every single treatment. Dose escalation has been made feasible due to this improved accuracy which has allowed better therapeutic ratios for a number of tumor sites, such as prostate and head and neck cancers [2].

2.1.1.5 Stereotactic body radiation therapy (SBRT)

SBRT has the possibility to precisely deliver very high radiation doses over a low amount of treatment fractions. This can provide ablation of well-defined, small tumors originating on any location in the human body. Tissue adjacent to the tumor has a likely chance of receiving damage due to the high dose [2].

However, clinical significant toxicity remains low when the normal tissue amount in the region of high dose is non-eloquent and small. SBRT has depicted fantastic results when early stage non-small cell lung cancer is treated in non-operable patients [2].

2.1.2 Treatment planning

In order to calculate the correct dose distribution for any radiation treatment, one needs a treatment planning system (TPS). The dose distribution calculated by the TPS subsequently has to be verified using QA tests. A radiation therapy system delivers radiation by means of monitor units (MU), where the dose per MU is determined under specific calibration conditions for the medical linear accelerator (linac). Most commonly the reference conditions are a 10 cm by 10 cm field with an SSD of 90 cm at a depth of 10 cm of water with one MU being equal to one cGy [11], [12].

Maximizing the ratio between the TCP and the healthy tissue complications probability, known as the therapeutic ratio, is the aim of treatment planning in radiotherapy. Due to rising advancements in TPSs, improvements on techniques of radiation delivery and the rise of new modalities for imaging for localization and delineation of organs at risk (OAR) and tumors, the aforementioned ratio has been increasing continuously [13].

In order to first structure targets in a patient's body and to calculate the dose distribution afterwards, the data from computed tomography (CT) needs to be imported to the TPS. To calculate an accurate dose distribution, calibration of CT numbers needs to be performed using various tissue substitutes in a phantom for calibration. There are generally two methods for this type of calibration for photon radiation therapy, namely the CT number to mass density calibration and the CT number to relative electron density calibration. The calibration curve for the conversion is specific for the used CT-scanner. This curve is obtained by calibrating the CT-scanner with the use of a water equivalent phantom. The phantom contains various materials of which the densities are known and are equivalent to the densities of different tissues. Both methods change dependent on the used TPS and dose calculation algorithm [14].

When external beam radiotherapy is utilized it can be generally noted that the absorbed dose in the patient can be affected or altered by the introduction of certain heterogeneities by various types of materials such as lungs, bones and air. These materials have Hounsfield Unit (HU) values that are either very low or very high. This effect is most pronounced when using small or irregular irradiation fields. Treatment planning systems have been utilizing more complex and advanced dose calculation algorithms to access more accurate calculations and representations of the absorbed dose in the patient [15].

2.1.2.1 Dose to water calibration

Photon beam radiation therapy usually reports the absorbed dose to water using conventional dose calculations. The reason why the reporting is done in dose to water has two primary reasons. The first is due to historical developments of algorithm used in treatment planning systems and the second is because of the fact that the calibration of treatment machines is performed in terms of absorbed dose to water applying a water phantom. A water phantom having a side length of approximately thirty centimeter with walls made out of plastic is recommended which is consistent with secondary standard calibration phantoms [16].

For the calibration it is necessary to first assemble and control the equipment such as the ionization chamber, electrometer, thermometer and barometer. The used water phantom needs to be positioned on the same axis in line with a ^{60}Co source. The collimator setting and the distance from the water phantom to the ^{60}Co must be set accurately. When a source to surface distance of one meter is used an uncertainty of 0.5 mm in position of the phantom an uncertainty of approximately 0.1 % will be added to the calibration coefficient [16].

Five centimeters of water is typically the reference depth in ^{60}Co (provided the phantom has a plastic window this is expressed as 5 g/cm^2), combined with a dose gradient of about 0.5 % /mm, the positioning of the ionization chamber should be performed with an 0.2 mm or less uncertainty in order to not contribute more than 0.1 % to the calibration coefficient. A suitable range for the electrometer range needs to be selected while disabling any auto ranging function. An irradiation time should be selected that will give reading of the electrometer that is reasonable, which lies typically between twenty and a hundred seconds. The effective time depends on the activity of the ^{60}Co source and the chamber volume [16].

After a series of ten readings, the mean and the standard deviation of the mean are computed. The pre-calibration leakage should also be added to the calculations. This process is repeated for a minimal of three more sets while noting the pressure and temperature for each set. The mean values should then be normalized to the standard temperature and pressure conditions chosen for the calibrations. The leakage occurring after calibration should be remeasured with a correction performed for the mean values, using an average of the leakage before and after calibration [16].

Because of this dose to water calibration process, treatment planning systems handle different density voxels as water with variable electron density. This gives a relatively good representation of the dose that would be absorbed by the patient because of the fact that water makes up most of the tissue and volume found in the human body. However this does not take into account tissues with very high or very low density like bone or air [17].

2.1.2.2 Dose calculation algorithms

There are three generations of algorithms that have been used throughout the history of dose distribution algorithms. Type A algorithms handle heterogeneities in the irradiated body by solely utilizing the longitudinal direction to scale the beam density. One of the type A algorithms is pencil beam. They were quickly replaced by another category of dose calculation algorithms, called type B algorithms. The dose delivery is estimated by calculating the density of the surrounding tissues through collapsed cone convolution This is called a kernel-based model, containing a nominal model for lateral scatter [15], [18].

The most recent advancement in photon dose calculation algorithms is implemented in the Eclipse TPS which is produced by Varian Medical Systems. As opposed to commonly used type B-algorithms which are kernel-based, or Monte Carlo methods which use a statistical approach, the Acuros XB Advanced Dose Calculation (Acuros XB) solves the Linear Boltzmann Transport Equation (LBTE) in a deterministic way. This type of solver is said to produce distributions of dose with an accuracy equivalent to Monte Carlo algorithms, which allows for a more accurate modeling of the dose deposition in a certain type of medium. The LBTE thus describes the behavior of radiation particles as they react with or pass through matter. It is already shown that algorithms that allow the calculation of dose-to-medium tend to lead to better agreement with Monte Carlo calculations [5].
Acuros consists of two different dose reporting methods: First there is the dose-to-water (AXB_W) method and second the AXB_M method. Regarding the electrons, the fluence-to-dose response functions are applied which are dependent on the related energy. By these means the dose can be obtained in all different voxels. When dose to medium is used, the cross-section of the macroscopic energy deposition and the atomic density are determined using the correct material properties of the corresponding voxel. This is done by taking the HU from the CT-scans, converting them to mass density by utilizing the calibration curve. Hereafter, the mass density is mapped to biological or non-biological materials. By using dose to water the corresponding media deposition cross-sections are utilized [5], [19], [20].

When Acuros is utilized, the errors that will occur are prominently systematic. These occur because of the solution parameters that are discretized in energy, space and angle. Because there was always a desire to shorten the calculation time of Monte Carlo simulations or to find another simulation method that proves to be a rapid alternative to the Monte Carlo code, the development of deterministic LBTE solvers was started [17], [20].

Concerning energies in the low MeV range (smaller than 25 MeV), Acuros proves to deliver an accuracy that is equivalent to that of the Monte Carlo simulations. This accuracy is effective when using clinical (linac) for a high range of materials and densities [17], [20].

Acuros also provides a determination of the materials in the patient or phantom in the Eclipse TPS. This is done by first reading the HU of the voxels in the CT-image. The HU image is converted to a mass density image using the mass density calibration curve of the CT-scanner, provided by the user of which an example is presented in Figure 1. After this a conversion is performed in which the mass density is converted to a mixture of five possible types of tissue retrievable in the human body, which are lung, adipose tissue, muscle, cartilage and bone plus air. Figure 2 depicts the physical materials table from AcurosXB-11.0. Automatic HU to material conversion (AutoHU2Mat) is only performed for those six materials. When a density is calculated which lies between the minimum and maximum of two separate tissues it will be converted to a mixture of those two tissues. For example: a CT-value of 734 HU will be converted to 1.446 g/cm^3, which results in a mixture of 31 % cartilage and 69 % bone [21].

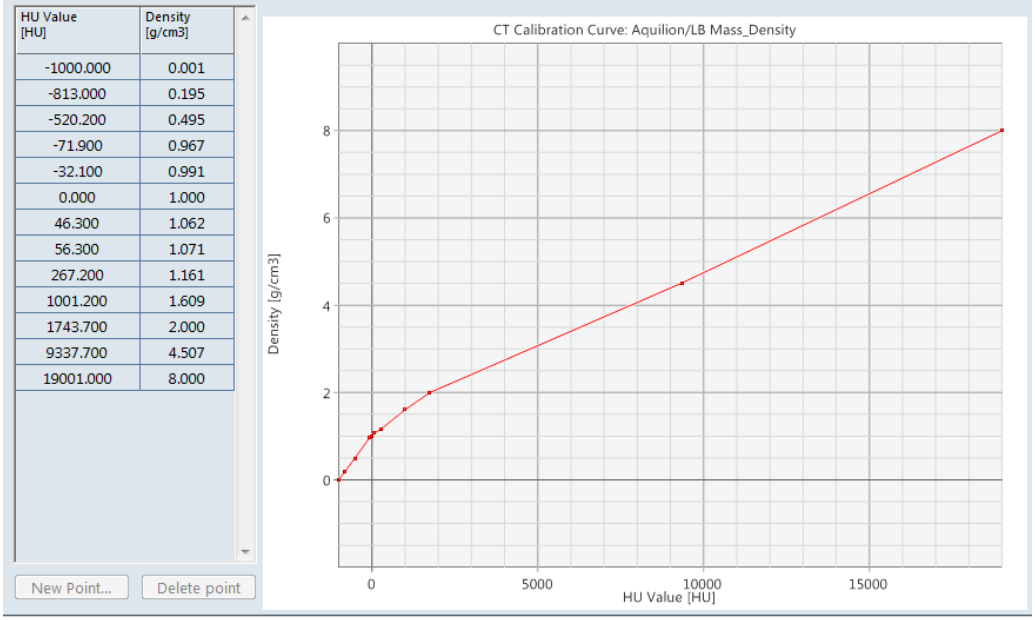

Figure 1: Mass density calibration curve used by Acuros of a certain CT-scanner [21]

ID	Name	Min. g/cm^3	Max. g/cm^3	Def. g/cm^3	AutoHU2Mat
Air	Air	0.0000	0.0204	0.0012	Yes
Lung	Lung	0.0110	0.6242	0.2600	Yes
Adipose	Adipose Tissue	0.5539	1.0010	0.9200	Yes
Muscle	Muscle Skeletal	0.9693	1.0931	1.0500	Yes
Cartilage	Cartilage	1.0556	1.6000	1.1000	Yes
Bone	Bone	1.1000	3.0000	1.8500	Yes

Figure 2: AcurosXB-11.0 physical materials table [21]

In case a phantom is CT-scanned containing inserts of various densities and the materials are determined automatically by Eclipse, deviations of the dose may occur. The voxel HU value does not say anything about the materials chemical composition. This is especially true for phantoms using "exotic" materials. The same HU numbers may be depicted by two different materials, although the chemical compositions, and therefore the atomic interactions, can differ. In these instances it is advised to assign a material to a structure provided it is retrievable in the physical materials table of ARIA [21].

2.2 Dosimetry

2.2.1 Dosimetry phantom in radiotherapy

Historically tissue-equivalent materials have been used in the construction of anthropomorphic phantoms. The attenuation characteristics for studies concerning radiation dosimetry and the physical representation of human bodies are provided by these phantoms. Physical phantoms give the possibility to quantify organ doses which gives an advantage over computational methods since knowledge concerning the exact geometry of the irradiation and the photon energy spectrum is not necessary. Typically three sorts of tissue equivalent materials are used in phantoms that are commercially available. These are materials that mimic soft tissue, lung and bone. The RANDO (The Phantom Laboratory, Salem, NY) and ATOM (Computerized Imaging Reference Systems, Inc, Norfolk, VA) phantom are used primarily for diagnostic imaging studies and are assembled in 2.5 cm thick axial slices in order to be able to place dosimeters in between. The limitation concerning these types of phantoms is their prohibitive costs ranging upwards of 16 000 euro [6].

In ensuring safe and effective treatment for patients, dosimetry phantoms play an important role. The spatial distribution of absolute dose throughout the human body of a patient is an extremely important factor for the successful use of therapeutic EBRT. To ensure that the planned and delivered dose distributions are as equal as possible, the use of dosimetry phantoms in radiation therapy is critical. First, the calibration and characterization of delivery devices is controlled using phantoms. Secondly, by applying phantoms for dosimetry prior each radiotherapy course, they offer a verification method for the planned and calculated dose distributions of the treatment plans. As a rule the phantom itself is a conventional human body model or has a simple geometric shape. Plastic approximating the density of different tissues in the human body is used in the fabrication process of modern phantoms [3], [4].

2.2.2 Alanine (EPR)

A very suitable method for dosimetry where the dosimeter has to be positioned in a region of interest (ROI) is the use of alanine ESR or EPR dosimetry. Electron spin resonance (ESR) refers to the same form of technique used for electron paramagnetic resonance (EPR) and electron magnetic resonance [22].

Dosimetry using alanine, specifically L-α alanine has been around for over 50 years. The alanine used for this purpose has irradiation-sensitive properties. The dosimetry is done by means of electron paramagnetic resonance (EPR) which embodies a number of very useful properties. In this type of dosimetry there is no dose rate dependence, low dependence on the energy of photon or electron beam and low dependence on the temperature of the irradiation.

It is a non-destructive technique and the EPR signal is highly resistant to fading when reading out the alanine. When a dose below 2 Gy is used, the signal obtained by the dosimeter will fade due to background radiation and noise. At a dose of 10 Gy this background influence becomes less than 1 %. At a dose of 2 - 10 Gy to 5 kGy a linear relationship between amplitude of the EPR signal and dose is obtained [23], [24].

When using alanine for dosimetry using beam energies used in radiation therapy, it will not cause any discontinuities or disturbances because of the fact that alanine provides great tissue equivalency. It is suggested that the uncertainty of the delivered dose should be less than 3% so as to obtain a correct correlation of the prescribed dose with the effectively obtained dose for the patient [23].

The chemical name of alanine is 2-aminopropanoic acid with following molecular structure: $CH_3CH(NH_2)COOH$ which is made up of a methyl group (CH_3), an amino group (NH_2), a carboxyl group (COOH) together with an extra hydrogen atom which are bound to a central carbon atom. This makes it one of the most simple and small acid participants of molecular biosynthesis. Alanine can be differentiated from other amino acids via the methyl group. An important notice is that it can exist in two forms who are isomeric to each other. These are the D-alanine and the L-alanine. A mixture is also possible which would make DL-alanine. The forms that should prove important for dosimetry are the L-alanine and DL-alanine [22].

When alanine interacts with ionizing radiation, radicals are formed. When the bond of the NH_2 group breaks an unpaired electron is created and together with the central carbon atom paramagnetic properties are achieved. Combine this with hyperfine interactions that occur due to the presence of the unpaired electron with the radical CH_3-C·H-COO, especially the hydrogen atoms of which there are four, gives an unique EPR spectrum visualized in Figure 3 [22].

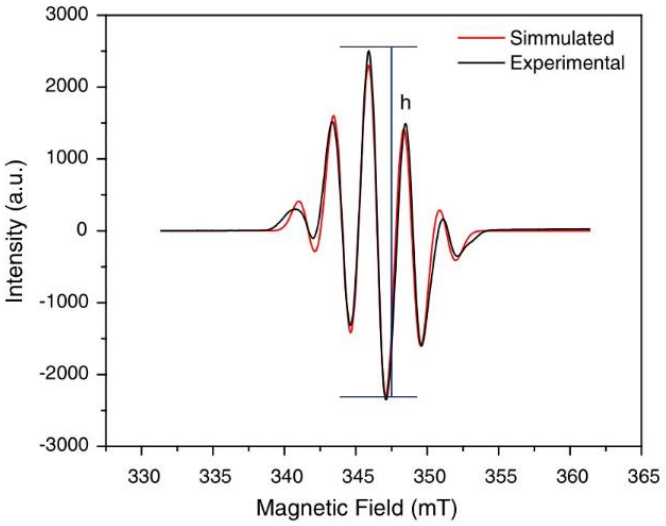

Figure 3: EPR spectrum of L-alanine irradiated with 150 Gy. The calibration curve is set up using the amplitude noted with h [22, p2]

So when using alanine (EPR) dosimetry the amount of paramagnetic centers created by the used ionizing radiation can be detected and visualized as an ESP/EPR spectrum [22].

2.2.2.1 Peak-to-peak method

The concentration of the produced unpaired electrons is determined by the recording of a ESR/EPR spectrum. Since the purpose of this is calculating or measuring the absorbed dose, the amplitude h of the most significant line in the spectrum can be directly correlated to the dose provided the microwave power and modulation amplitude are kept exact [22].

2.2.2.2 Amplitude method

A background spectrum (un-irradiated pellet) is subtracted from the spectrum of the alanine pellet irradiated with an unknown dose and from a EPR spectrum irradiated with a known dose. A base function is plotted in which the intensities between the central peaks of the EPR signal are set out to the corresponding intensities in the reference spectrum. The resulting slope then determines the ratio of amplitude between the unknown dose pellet and the known spectrum. This slope can then be multiplied with the known dose which gives a first estimate of the received dose. Using a least-square fit of the highest R^2-value segment gives the respective slope. This has the primary advantage of not being sensitive to small x-axis shifts because that will only cause an offset but no slope change [25].

2.2.2.3 Uncertainties

Concerning radiation therapy, there is a requirement of a small uncertainty when measuring the applied dose. One uncertainty originates from a calibration irradiation by a primary or secondary standard dosimetry laboratory [22], [26].

A second one is due to the uncertainty that is expected by the ESR readout itself. The humidity and room temperature can have an indirect impact on the amplitude of the EPR signal by the irradiated alanine. The aforementioned environmental conditions could affect the background signal an temporal evolution of the ESR signal. With all this factors included a precision of 0.5% could theoretically be achieved for doses ranging from 5 to 25 Gy for probes irradiated with ^{60}Co and 1.0 % for pellets irradiated with 4 Gy [22], [26].

2.2.3 Gafchromic film (EBT3)

Radiochromic films are very often used for patient-specific dose verifications and a wide variety of radiotherapy treatment methods and modalities. They contain a sensitive medium that is not broken throughout the entire film. Moreover, they also provide a very high spatial resolution and due to their near water equivalence, they do not show an overwhelming response due to low-energy photons. Furthermore, they show no volumetric averaging effects and act as natural 2D dosimeters in contrast to ionization chambers and silicone diodes. In addition, they can be irradiated in any position and they can be used with any phantom where they generate very little perturbation of the beam fluence. With gafchromic films like EBT3 films, no post-irradiation processing such as chemical development is required and there is no energy dependence, unlike traditional radiographic films [27], [28].

The EBT3 films are produced similar to EBT2 films with similar performances. The advantage of the latest version of EBT films is that the layers are arranged symmetrically with the effective measuring point at the center of the film. It contains a single active layer which contains, with the active component, stabilizers and marker dye . All of these and some extra additives makes for a film with low-energy dependence. Since the dynamic range is designed specifically to perform optimally in a dose range from 0.4 to 40 Gy, it is most suitable for use in stereotactic radiosurgery (SRS) and stereotactic body radiation therapy (SBRT). They also contain an anti-Newton ring artifacts coating. These normally occur as a result of light interference on reflection between the different surfaces of the film, where the distance between them is small but varies [29].

When the EBT3 film is irradiated, the active component inside reacts to the given radiation and forms a polymer with a blue colored polymer that has an absorption maximum at 633 nm approximately and polarizes transmitted light. When using a flatbed scanner this polarized light is transmitted to the film and guided to a CCD detector utilizing a lens and a series of mirrors. It is recommended that the gafchromic film is used with a 48-bit (16-bit per channel for the three color channels) flatbed color scanner. The appropriate color scanners measure the red, blue and green color components given by the light which the film transmits at 16-bit color depth. The calibration curves used on an Epson 10000/11000XL scanner should be fitted to a function of following form [30]:

$$d_x(D) = a + \left(\frac{b}{D - c}\right) \quad (1)$$

Where $d_x(D)$ represents the optical density (OD) of the film with a corresponding dose D, using scanner channel x. The letters a, b and c are the parameters that need to be fitted. This type of function has several advantages [30]:

- With respect to the physical reality this function has a rational behavior so that when an increase of density happens with an increase in exposure. However it shall approach a near constant value when higher exposures are reached. Contrary to polynomial functions which generally show no correspondence to physical reality when a range of data outside the fitting range is utilized;
- A fewer amount of calibration points are necessary due to the fact that the mentioned rational behavior is present. Due to this a significant amount of time and film can be saved. Typically six to eight points are used with the inclusion of an unexposed film while using geometric progressing doses;
- Using this function also provides a certain simplicity to determining and inverting density as a function of dose or the other way around, dose as a function density [30].

A lateral scan artifact (LRA) is exhibited by many flatbed scanners used for measurements for film of the radiochromic nature. This artifact happens when varying color values occur depending upon the relative placement location of the film to the center of the scanner. Film that is scanned on a location further away from the center will show a greater OD which will then be converted to a higher calculated dose. When the dose is increased this deviation shall also increase [30].

2.2.3.1 One-scan method

This new measurement protocol for patient dosimetry or application films functions differently from the typical practice in which the application scan is scanned alone. This method combines the digitation of two reference or calibration films with the digitation of the application film. All used films are scanned together in a single scan and are from the same production lot. For the reference films one film is not exposed to radiation while another is exposed to a certain set and thus known dose. The dose-response function can be adjusted, rescaled or recalibrated by the data provided from the reference films measurements to adapt for the specific conditions for one particular scan. This has several advantages, differences of the scanner between calibration and the actual measurement is eliminated along with temperature variability and it is possible to obtain results within 30 minutes. This is due to the fact that all films (application and reference) are exposed is a short amount of time so the scanning and analysis can be finished in a short time frame. This method delivers a faster and more efficient work flow with accuracy enhancements of the results [31].

2.2.3.2 Uncertainties concerning EBT3 film dosimetry

There are many causes of uncertainties when using film dosimetry. These can therefore be classified into a number of categories: The development and manufacturing, manipulation, irradiation, digitization and film response characterization. In the production of the film, the homogeneity may vary throughout the entire film or in different versions of the film. During the manipulation, care must be taken when cutting or storing the film. The use of a certain phantom, the setup of the film, the phantom and so on creates uncertainties for the irradiation. Furthermore, the digitization of the film depends on the flatbed scanner used and the characterization of the film response with the absorbed dose depends on the fitting calibration function used [27].

When using EBT3 films it can be emphasized that a total uncertainty from previous described sources of approximately 2 % can be achieved at doses used in radiotherapy with photons and therefore have a value greater than 1.5 Gy. Scanning films produces optical density (OD) values that include a number of sources of uncertainty. In order to calculate the global uncertainty, these uncertainties must be quantified. The main causes of these uncertainties come from the measured dose for calibration of the films and the general uncertainty on the measured netOD [28]. The netOD can be calculated using the following formula:

$$netOD = log_{10}(\frac{I_{unexp} - I_{bckg}}{I_{exp} - I_{bckg}}) \quad (2)$$

In which I_{unexp} is the measured intensity for unirradiated films, I_{exp} the irradiated films and I_{bckg} is the measured zero-light transmitted intensity. The uncertainty on the measured dose is evaluated at less than 2 % when the prescribed protocol is correctly implemented, less than 1.5 % on the calibration curve for high energetic photons and protons considering the film reading and fitting [27], [28].

2.2.3.3 Individual color response

Figure 4 depicts the dose response curves for the all three color channels for a photon beam of 6 MV. The fitting dose-response curves for each color are represented by a solid line. It is clear that there is a different response to the irradiation for the three color channels. The most sensitive color channel can be chosen by calculating the first derivative of the fitted netOD with respect to the dose which in this particular case is the red color channel because of a steeper netOD to dose ratio (highest rise of netOD to dose value) [28].

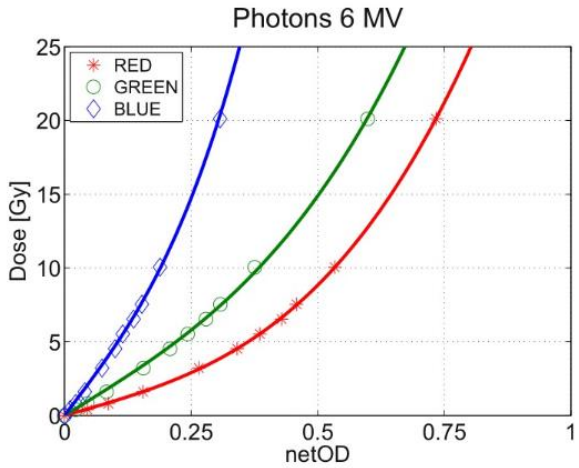

Figure 4: Dose-response curve for a 6 MV photon beam [24, p4]

2.3 3D-printing in medicine

In recent years, 3D-printers have already been used in medicine. Since the use of this technology for dental implants and the adaptation of prostheses, the technology is rapidly expanding and revolutionizing healthcare by using it for various purposes including organs, implants and anatomical models [32], [33].

According to the International Atomic Energy Agency (IAEA) Code of Conduct's Technical Report Series No. 457 (TRS 457), standard phantoms must be designed and manufactured to exhibit the same primary attenuation and production of scattering as the applicable sections of the body of a representative patient. Furthermore, when manufacturing a phantom, the energy range as well as the cost, availability and dimensional stability of the material must also be taken into account [34], [32].

The 3D-printing of anatomical structures based on data from medical images began in the early 1990s. These were mainly made for a number of purposes: planning of surgical interventions, patient education and prostheses which were meant for implantation. The process was also used to produce molds designed from CT images for tissues that cannot be printed by default by their nanoscale structure and to create hollow structures that provide vascular properties that can be utilized with phantoms used for currents [35].

3D-printing has already been used in a number of studies to fabricate phantoms for QA and dose verification. A kidney phantom can be created by using agarose in the phantom production [7]. Fused deposition printing technology has been used to manufacture anthropomorphic phantoms for measurements of radiation therapy dose [8]. With the use of a Polyjet printer, a chest phantom designed for dose detection inside lung tissue and also in- and outside a moving tumor has been fabricated [36].

When comparing CT reconstruction algorithms, a Polyjet 3D-printed phantom of liver tissue was already developed by using a texture model of which the parameters originated from real patient CT images [37], [38]. A 3D-printed MRI compatible head phantom has also been reported [39]. Furthermore, 3D wax-printing and polymer molding was combined in a novel technique in order to construct soft phantoms. In the studies on lung and bone tissues, small animal experiments and MRI, similar methods were found [10].

These previously reported methods are difficult and complicated to practically adopt for clinical use, despite the aforementioned advanced technologies. Furthermore, in terms of radiation attenuation the equivalency to the represented tissue of the previously utilized materials has not been proven. The applications in clinic of various anthropomorphic phantoms include surgical guidance, dose verification, QA, equipment calibration, teaching, and so on. Therefore, the phantoms should be designed containing attenuation characteristics and anatomy similar to human tissue [10].

2.3.1 Methods of 3D-printing

3D-printers that use additive production techniques build 3D objects by adding one layer on top of another. Two types used in the development of CT phantoms are FDM printers and Polyjet printers, the latter type of printer uses liquid photopolymer, deposited layer per layer and immediately cured by adding ultraviolet light. 3D-printers using the FDM technique use a solid filament to print. The filament is first melted, after which it is extruded through a spout and finally deposited on an earlier printed layer on which it adheres, cools and hardens relatively quickly. These types of printers offer a high spatial resolution of less than 1.0 mm which makes them a very attractive option, especially combined with the fact that these systems are low-cost and the printing materials can be cheap and easily accessible. For these types of printers there is usually no specific attention paid to the radiopacity even though there are many different types of materials available. PLA and acrolylonitrile butadiene styrene (ABS) are the two most common materials used in this type of printer and have radiopacities lower than that of water [32].

High impact polystyrene filament is commercially available to use with an FDM printer. With this filament type the possibility exists to develop low density phantoms for radiotherapy for use as quality control. Variations in the attenuation were obtained by using the infill percentage parameter of the 3D-printer. This allows the percentage of the inside volume of an object filled with printer material to be adjusted. The rest is naturally filled by air. The average attenuation values with this technique start at zero ranging up to eight hundred HU [37].

2.3.2 Filaments

The development of materials that produce tissue equivalency and are utilized in phantom construction intended for x-rays started as early as the 1900s. The first generation of such phantoms was based on wax. The wax phantoms contained radiopaque filters such as polyethylene, calcium carbonate, titanium dioxide and silicon dioxide. To adjust for the density in epoxy resin, phenol microspheres were added together with the above additives [37].

The two most commonly used and most viable filaments for the fabrication of a thorax phantom are ABS and PLA. ABS has already been investigated numerous times for the production of a medically useable phantom [40]. Tissue-equivalency is dependent on two primary factors, which are the CT-values, or the Hounsfield units (HU) on a CT-scan of the selected material and the effective relative electron density (RED_{eff}) which offers an adequate description of the radiological thickness concerning most printed materials combined with the attenuation of MV beams [41].

2.3.2.1 Acrolylonitrile Butadiene Styrene

3D-printing with ABS with a density of 1060 kg / m^3 can provide geometrically accurate and radiologically robust materials that could potentially be useful for lung and tissue equivalent phantoms. An ABS infill density of 90% can serve as a material to mimic tumor, muscle or other soft tissue. ABS infill densities of 30-50% result in phantoms with densities that are low enough to simulate lung tissue. This also avoids the mesh structures that occur with the use of even lower infill densities (e.g. with 10% ABS) [9], [41].

2.3.2.2 Polylactic Acid

When megavoltage CT (MVCT) images and 120 kVp images are reviewed it becomes notable that the CT-values of different infill densities of PLA-inserts correspond to those of certain tissues in the human body. Inserts of PLA with 90 % infill density have the same CT-values as the values between those for water and brain-tissue. When 80 kVp images are considered there is also a correspondence between the CT-values of the PLA with 90 % infill and the values of water within a certain uncertainty. Therefore, PLA with an infill density of 90 % could provide a close and useful equivalency for numerous sorts of soft tissue corresponding to CT-values of around 0 HU. Regarding lung tissue it is found that PLA with an infill density of 30 % approximates the CT-values of lung tissue which range from -700 to -600 HU. Since 100 % PLA has a mass density of approximately 1.21 g/cm^3 a 90 % infill would conform to the average mass density of human soft tissue (adipose/muscle) which has a value of 1.006 g/cm^3. 30 % infill would conform to the average human lung density of 0.386 g/cm^3 [14], [41].

2.3.2.3 Flexible filaments

3D-printed flexible materials such as Fullcure TangoPlus FLX930 and HeartPrint Flex show a similar strength compared to already used materials in vascular phantoms such as poly Sylgard elastomers (PDMS). Although the 3D-printed flexible material is less stiff under dynamic loading conditions, both materials can withstand cyclical loads very well. They also exhibit better tear resistance than the PDMS systems. This makes them ideal for pulsed short-term flow applications and for bench tests. They also contain the ideal material properties, especially transparency and scattering, for phantoms with ultrasound applications [42].

2.3.3 Issues regarding bone equivalency

Some problems occur when looking for a suitable 3D-printable filament that has bone-equivalent characteristics. Inserts made from PLA or ABS can never reach the desired CT-values corresponding to human bone. Therefore other materials like photopolymer resins are used. Regarding MVCT images these should provide good surrogates for bone tissue. However, a downwards shift of the CT-values is present when lower energies (80 – 120 kVp) are used for the imaging. This shift in CT-values causes the resins to resemble liver tissue instead of bone [41].

When scanning copper fill and bronze fill 3D-printed materials, which show a great equivalency to cortical bone in MVCT scans, with beams of 80 – 120 kVp a misrepresentation of the CT-values happens. The values of the metallic filaments lay outside of the normal range for body tissue, which ranges from – 1024 HU to + 3096 HU. This is most probably caused by artifacts that normally occur in kVCT images taken of metallic objects. However, it is possible to get a true estimation of the CT-values of 3D-printed metallic and other high density materials but only when using MVCT imaging [41].

2.4 RTV Silicone

Room temperature vulcanizing (RTV) silicone is a type of silicone rubber which is made from a bi-component system existing of a base and catalyst which can by definition vulcanize at room temperature. The catalyst that is used in the curing process of RTV silicones can consist of tin compound like dibutyltin dilaurate or platinum [43].

The hardness of this type of silicone ranges from very soft to a medium hardness. This type of product should offer an extremely high tear strength and a high accuracy in reproducing a product with very small details. Furthermore the silicone offers high dimensional stability and is practically indeformable. It is a silicone that is primarily used for the fabrication of molds and models which offers an ideal possibility in making asymmetrical objects like ribs [43].

2.4.1 Curing process

The curing process is a chemical process which is commonly used is process engineering and polymer chemistry. During the process polymer materials are hardened by cross-linking polymer chains. Oligomers and single monomers are mixed to form polymeric networks.
This can be induced with or without adding a curing agent. Firstly molecule branches are formed with different architectures. When the solubility is disappeared and the viscosity is enlarged the reaction has finished. The molecules that remain can start to coexist with the network that has been formed until reactions occur with that same network and new cross-links are formed. Until the very end of the chemical reaction the cross-linking density keeps increasing [44].

There are several possibilities and ways to initiate the curing process. These are: the addition of heat, radiation, electron beams or chemical additives. Two large classes can thus be distinguished. First there is the class in which the curing occurs when adding chemical additives and second there is the class that induces the curing process without the need of additives. With the use of rubber, the curing is primarily induced by the use of additives which are called crosslinkers. The process that happens with this crosslinking is referred to as sulfur vulcanization. Polysulfide cross-links are formed between the polymer chains sections by breakdown of the sulfur. Many properties of the resulting material are determined by the degree of crosslinking. Some important properties influenced by this are the rigidity and the durability [44], [45].

RTV silicone can be constructed when reactive polymers that are reactive oil-based are combined with mineral filter that have strengthening capabilities. Concerning RTV silicone there are two possible types which are the one-component systems and the two-component systems. The one-component systems experience a hardening process that can be caused by atmospheric humidity, the use of a catalyst or acetoxysilane. This type of curing process starts from the outer side and goes inwards to the core of the silicone. The two-component systems consist logically of two products that cure at room-temperature when they are mixed. At the end of the process a solid elastomer, a flexible foam or a gel is formed [46].

3 Method and materials

The practical study contains several parts to complete the final objective. First, a model of the phantom was designed using a 3D-modeling program. Secondly, a substitute to the bone equivalent material was searched for since it is practically impossible to find a 3D-printable filament that achieves the correct properties. When both the phantom was 3D-printed and the bone equivalent material was finished, they were combined to prepare for the imaging and dosimetry. Subsequently, the phantom was imaged using a CT-scanner after which a radiotherapy plan was created and the phantom was irradiated while EBT3 films and alanine pellets were positioned inside. Lastly, the dose absorbed by the film and the alanine pellets was calculated and compared to the radiotherapy treatment dose plan. The imaging and irradiation were performed at two clinics, the Maastro Clinic at Maastricht (clinic 1) and the Jessa hospital in Hasselt (clinic 2) with different setups and utilizing the one-scan method only in clinic 2.

3.1 Objective

This Master's thesis aims to investigate the possibility of constructing a 3D-printed thorax phantom containing equivalent material to the soft tissue, lung tissue and bone tissue found in the human thorax. With an important part being the examination of materials that could provide good bone equivalent characteristics for both imaging and dosimetry. This phantom should serve as a low-cost and easy to fabricate alternative to the conventional thorax phantoms used in radiotherapy and thus with megavoltage energies.

3.2 3D-printed phantom: modeling and construction

The 3D-printed phantom first had to be designed using an 3D-modeling program. The program used was Autodesk Fusion-360. Since I had zero experience with 3D-modeling or the use of the particular software, this was an important part of this thesis which took up a lot of time.

3.2.1 Designing the thorax phantom

It was very important to have insight into what the finished phantom should look like and how it should function concretely, even in the first step of realizing a 2D representation containing all final parts. Because the phantom (lungs not included) would eventually consist of four parts, it was taken into account during the modelling that all parts would finally fit together without problems.

Secondly, a 3D-volume had to be created. This could not be done simply by extruding the 2D drawing as there had to be notches for the ribs. The ribs were modelled in such a way to obtain the best possible representation of human ribs. The top side of the inserts was modeled rectangular and the bottom side was modeled rounded. A 3D-view, top view and side view of the rib design is visualized in Figure 5 to Figure 7

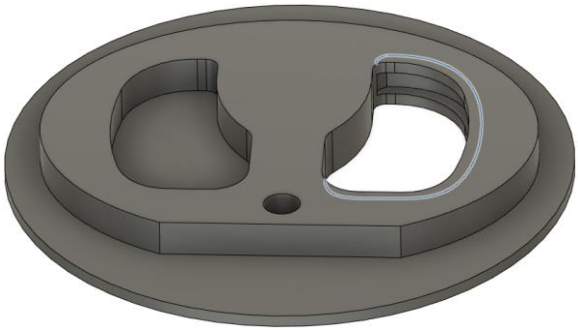

Figure 5: 3D-design first right rib with no rounded edges

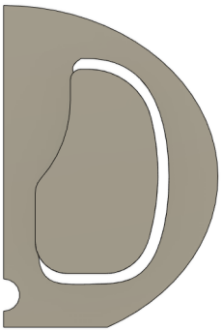

Figure 6: Top view rib design

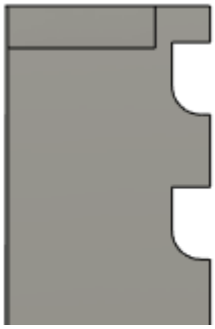

Figure 7: side view rib design of two ribs depicting rounded lower edge

Furthermore, space had to be provided for both the alanine pellets and the EBT3 films. The phantom, not containing the lungs or spine, was divided into four parts. The lungs were also divided into two parts at the same region were the soft tissue equivalent material surrounding the lungs was divided, so that a film would fit completely through the phantom.

3.2.2 Design of rib and spine molds

In order to make ribs and a spine that would fit in the 3D-printed phantom, molds had to be designed to let the silicone mixed with $CaCO_3$ cure in the correct forms. This was done by taking the design of the thorax phantom and cutting out one rib of each side and doing the same for the spine.

In regards to dosimetry, it was not possible to completely fit an alanine pellet in a rib due to size restrictions, so this was consequently not done. However, the spine did have a large enough circular circumference to fit in alanine pellets.

3.2.3 3D-printing

To print the thorax phantom in PLA, an Ultimaker 3 device was used at the Makerspace at UHasselt. The first version of the thorax was designed with dimensions that were too large for the 3D-printer used. Consequently, it had to be printed on a scale of 75% of the designed dimensions.

All settings used for the printing process of the 3D-printed thorax are retrievable in Table 1. To achieve equivalency to soft tissue and lung tissue, infill densities of respectably 90% and 30% were used.

For the molds a lower infill density was utilized since these are not important for imaging or dosimetry and a low infill density gives enough structural strength. The total printing process has taken up a couple of days since the largest structure had the highest infill density.

Table 1: Parameters for 3D-printing

Layer height (mm)	0.1
Infill (%) lungs	90
Infill (%) soft tissue	30
Support	no
Adhesion	yes

After the printing process was finished the phantom had to be sanded first using sanding paper with a big grain after which the finishing touch was done using small grain sanding paper. The rib insertions had to be cleaned and residual parts of the PLA which were molten in place during the 3D-printing process had to be removed using small files.

3.3 Bone equivalent material

In the search of an alternative for bone with the right characteristics for imaging and dosimetry in radiotherapy that can be combined with the 3D-printed thorax phantom, two types of silicone were investigated. Bluesil Rhodorsil RTV (from here on further named as silicone type 1) was the first silicone that was tested. The second type of silicone was ZA 00 Translucido (further referred to as silicone type 2) and is visualized in Figure 8 and Figure 9. Both of the RTV silicones consist out of a catalyst and a base that need to be mixed before it hardens.

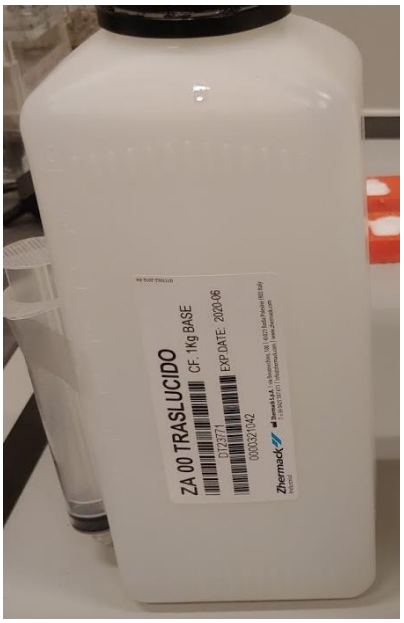

Figure 8: Base part of silicone ZA 00 translucido

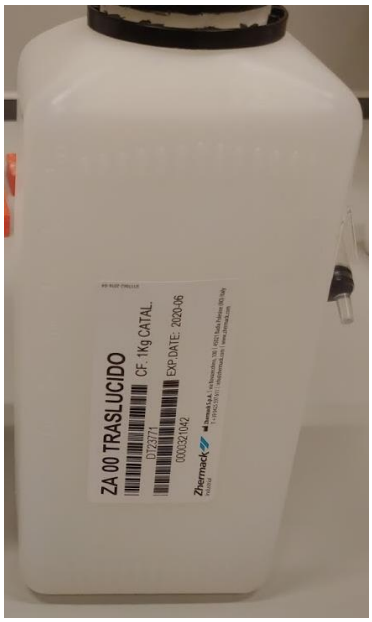

Figure 9: Catalyst part of silicone ZA 00 translucido

To create a bone equivalent material, the silicone had to be combined with a substance which contains high amounts of calcium, since human bone consists of 50% minerals of which 64% is calcium [47]. The chemical compound that was chosen for this was $CaCO_3$. This was easily accessible and has a high calcium percentage. Figure 10 shows the used precipitated $CaCO_3$, which is fabricated by first hydrating calcium rich quicklime and secondly making it react with carbon dioxide and was available at the UHasselt. One issue with this was that there was no datasheet available. The original purity when it was purchased was confirmed to have been around 98-99% since it is meant for analyses purposes.

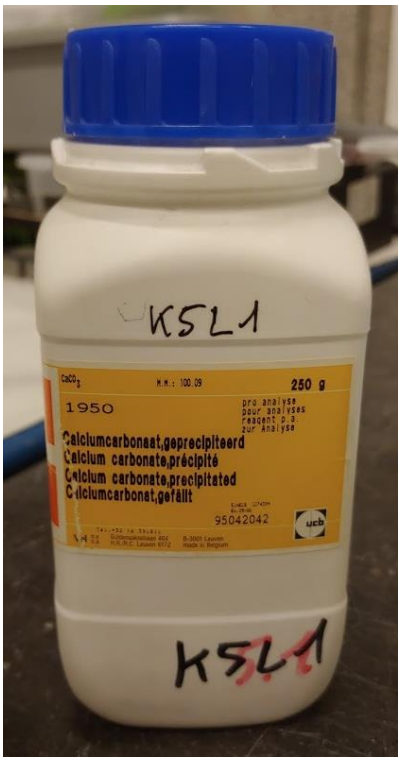

Figure 10: $CaCO_3$ used for fabricating bone equivalent material

3.3.1 Imaging properties

The first property that needs investigating were the CT-values achievable by the alternative to bone compared to real bone tissue. To determine the exact CT-values of the specific bone types needed for this experiment, real patient CT-images were reviewed using dedicated software (3D-slicer version 4.10.2 and RadIant DICOM Viewer). Different regions of interest were used to achieve a mean CT-value of both the ribs and the spine in the thoracic region. A human spine is naturally more dens on the back part which consist primarily out of the processus spinosus, processus transversus and the lamina. The front part of the spine (corpus) is less dens since more bone marrow is present. As a result of this; it would be ideal to experiment with the silicone to have a more dens front part and less dens back part.

Both of the silicone types were first off all mixed with an unmeasured amount of $CaCO_3$ to be able to view the homogeneity using a CT-scan (Siemens SOMATOM Confidence). The goal here was to find a silicone that cures rapid enough so the $CaCO_3$ did not sink to the bottom and thus achieves a high homogeneity within the silicone. Table 2 shows the properties of both silicones including the curing time (time it takes to completely harden and thus can be removed from the mold) which shows a significant difference when comparing both of the silicones.

For both silicones the curing time is reduced when the temperature is increased. For this thesis the choice of silicone will primarily be dependent on the imaging capabilities and thus the homogeneity of the $CaCO_3$ in the silicone when mixed and cured.

Table 2: Properties of both types of silicones used

	BLUESIL RTV-141 (silicone type 1)	**ZA 00 TRANSLUCID (silicone type 2)**
Mixing ratio (base to catalyst)	10 to 1	1 to 1
Mixing time	/	1 minute at 23°C
Working time (WT)	/	6 minutes at 23°C
Setting time (ST)	4 hours at 65°C	50 - 60 minutes at 23°C
Tensile strength (N/mm^2)	6.2	1.07
Elongation at break (%)	115	550
Tear strength (N/mm)	4.9	5

Thereafter, the chosen silicone (silicone type 2) was tested containing various amounts of $CaCO_3$ to find the correct CT-values that correspond to human ribs and spine. This was done by consistently mixing 5 ml of base with 5 ml of catalyst, respecting the mixing ratio of 1 to 1, for ten times using syringes of 5 or 10 ml. The amount of $CaCO_3$ added was increased each time. The amounts used were: 3 g, 4 g, 5 g, 6 g, 8 g, 10 g, 12 g, 14 g and 16 g. the influence of changing the amount of silicone was tested by mixing 10 ml of base with 10 ml of catalyst and adding 20 g of $CaCO_3$. The silicone was poured into 3D-printed molds that were used as tumor molds in previous performed study. Once the silicone was cured, the samples were taken out and a marker was written on each one correlating to the amount of $CaCO_3$ they contained which is shown in Figure 11 and Figure 12.

Figure 11: Samples of silicone mixed with $CaCO_3$ with five samples curing in 3D-printed tumor molds

Figure 12: Ten cured silicone samples containing various amount of $CaCO_3$

When all ten samples were finished they were scanned using a CT-scanner and reviewed using Radiant DICOM Viewer 5.0.2 to identify the correct amount of $CaCO_3$ needed in order to achieve the wanted range of HU to mimic the ribs and the spine. Once this was completed the process of fabricating the rib and spine equivalent material using the most useful type of silicone could commence.

3.3.2 Bone density

The second property that has importance in the correct representation and correct dose distribution in radiotherapy is the density of the bone and thus also the bone equivalent material.

For the bone equivalent material made out of silicone, the density was measured using a graduated cylinder of 100 ml. A total amount of silicone of 30 ml (15 ml base and 15 ml catalyst) was poured into the graduated cylinder with an addition of the amount of $CaCO_3$ to reach the HU of the ribs and the front part of the spine which have a similar CT-value and subsequently with an amount that corresponds to the HU of the back of the spine. The density was then calculated by weighting the mixture and using the following formula:

$$\rho = (\frac{m}{V})$$

Where ρ depicts the density in g/m^3, m depicts the total mass of the mixture in grams and V depicts the volume converted to cubic meter.

Eclipse ARIA® (version 15.5) offers a method of analyzing different parameters of a selected part of the scanned volume when a treatment plan is designed. These parameters concern the CT-value, the mass density, the relative electron density, the relative proton stopping power and the physical material composition decided on the combination of all previous parameters. Consequently a control for the density can be performed according to these values.

A control was performed in order to validate the relative electron density (RED) of the bone equivalent material using the relationship between CT-value and RED depicted in Figure 13 and the electron density to mass density conversion factor (C) depicted in Table 3.

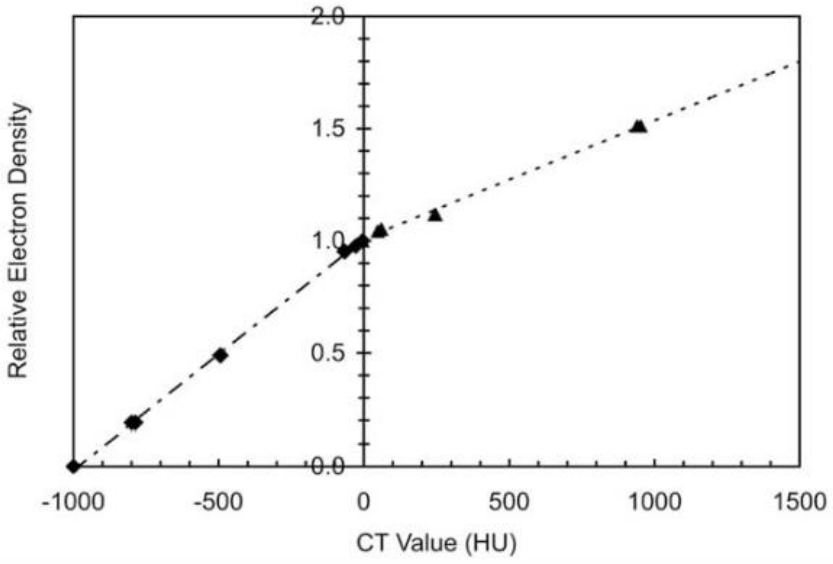

Figure 13: Relationship between measured CT-values and relative electron density [48]

Table 3: Conversion factor C for conversion of electron density to mass density of several different tissues [25, p48]

	$\bar{\rho}$(g/cm^3)			$\bar{\rho}_e/(\rho_e)_{H_2O}$			$C = \bar{\rho} \times (\rho_e)_{H_2O}/\bar{\rho}_e$ (g/cm^3)		
Classified tissue group	AM	AF	Average	AM	AF	Average	AM	AF	Average
Lung	0.385	0.385	0.385	0.382	0.382	0.382	1.009	1.009	1.009
Adipose/Muscle	1.012	0.998	1.006	1.006	0.994	1.001	1.006	1.004	1.005
Cartilage/Spongy-bone	1.112	1.112	1.112	1.096	1.096	1.096	1.015	1.015	1.015
Cortical bone	1.92	1.92	1.92	1.784	1.784	1.784	1.076	1.076	1.076
Tooth	2.75	2.75	2.75	2.517	2.517	2.517	1.092	1.092	1.092

3.3.3 Rib and spine fabrication

Along the process of modeling and designing a 3D-printable thoracic phantom for use in radiotherapy, molds for the ribs and the spine were also fabricated. These molds were filled with silicone containing the amount of $CaCO_3$ that produces CT-values in the range of the Hounsfield units of human ribs and spine.

Mixtures of 5 ml base and 5 ml catalyst were used. These were then set aside to cure for a period of about two hours each to ensure that the silicone was sufficiently cured after which they were removed out of the molds.

The back part of the spine was fabricated using more $CaCO_3$ as to achieve higher HU in order to mimic the back part of the human spine. Some retouching had to be done to ensure all ribs and the spine would fit in the phantom.

3.4 Dose verification and comparison

3.4.1 Irradiation setup

After 3D-printing and adjusting the phantom, it was time to scan and irradiate it. When the EBT3 gafchromic films (lot nr. 10151802) and alanine pellets (AR 388) were fitted in the phantom, it was closed and shut tight using adhesive tape. It was very important that every part of the phantom including the EBT3 films and the alanine pellets did not move when transferring the phantom from the CT-station to the linac-station. Furthermore, since the EBT3 films demonstrate some sensitivity to light, the films were covered or kept safe in an envelope when removed from the phantom. Although the EBT3 films are light sensitive, they are by far not as sensitive as argentic films commonly used in analog photography.

First of all, the thorax phantom had to be scanned by means of a CT-scanner (clinic 1: Siemens SOMATOM Confidence, clinic 2: Philips brilliance CT big bore) that could determine the HU of the lungs, the soft tissue and the bone. It is important that the position of the phantom in the CT scanner is exactly the same as the position of the phantom during irradiation. References to this placement were indicated on the phantom itself utilizing the laser positioning system (Figure 14). The parameters of the CT-scan for both clinics are depicted in Table 4.

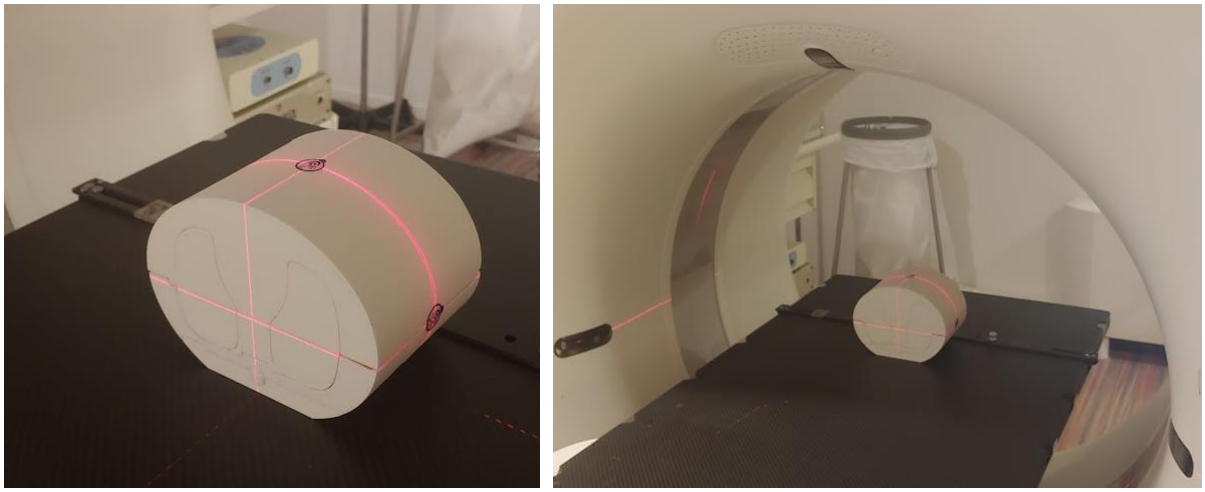

Figure 14: Positioning of the thorax phantom in the CT-scanner with reference points

Table 4: Settings CT-scan thoracic phantom

	Clinic 1	Clinic 2
Pitch factor (ratio)	0.8	0.8
Peak kilovoltage (kV)	100	120
X-ray tube current (mA)	167	321

3.4.2 Radiation therapy treatment plan Clinic 1

After performing the CT scan, a radiotherapy plan had to be designed on the basis of the CT-images. This was kept quite simple. An energy of 6 MV was used, giving three fractions of 2 Gy with a field of 10 by 10 cm^2 and a source to surface distance (SSD) of 93.3 cm. In order to make a comparison of the alanine pellets with the RT dose plan, a separate volume was delineated for each of the 14 pellets. These were named as NS-control to NS-control 13. The dose calculation algorithm used for the calculation of the TPS dose plan was AXB$_M$.

Once this was done, the plan was exported to the linear accelerator where the phantom was placed in an identical position as used during the CT-scan and the irradiation was performed. The position of the thoracic phantom in the linac (True Beam, Varian medical systems) is presented in Figure 15.

Figure 15: Positioning of the thorax phantom in the linac with visible reference points

3.4.3 Radiation therapy treatment plan clinic 2

The CT-scans were exported to the radiotherapy treatment planning system after which an irradiation plan could be designed. A beam energy of 6 MV was utilized, producing 6 Gy of dose in 1 fraction. A field of 5 by 8 cm was used in order to have complete coverage of at least 2 films (the middle film had too small dimensions).

The iso-center was shifted to the right side of the phantom in order to irradiate the most amount of alanine pellets possible considering the field size. This also ensured complete coverage of the spine together with a large part of one lung. In order to make a comparison of the alanine pellets with the RT dose plan, a separate volume was delineated for each of the 14 pellets. These were named as NS-control to NS-control 13. The dose calculation algorithm used for the calculation of the TPS dose plan was AXB$_M$. The same principles as in clinic 1 applied to the positioning of the phantom in the linac (Clinac, Varian medical systems). The dose calculation was first performed using a calculation grid of 2.5 mm. Since the ribs have a width of only about 7.0 mm the calculation grid was ultimately adjusted to 1.0 mm. The big difference to the irradiation in clinic 1 was that the one-scan dosimetry method for the EBT3 films was used.

3.4.4 Dose verification with alanine using EPR

This method was identical for both clinics. A total of fourteen alanine pellets (Harwell, Oxfordshire, UK; ø = 4.8 ± 0.1 mm; h = 2.7 ± 0.01 mm, m = 59.8 mg) were placed in the 3D-printed thorax phantom. They have a composition of 90.9 % L-α-alanine to 9.1 % paraffin (highest EPR signal). The notches in the thorax phantom were made during the design phase so that they no longer needed to be produced after 3D-printing. Only the pellets that were in the spine itself had to be protected because the alanine may not come into contact with the silicone (the fat of the silicone can be absorbed by the alanine pellet and later deposited in the spectrometer which causes contamination). This protection concerned a thin layer of plastic foil.

The alanine pellets were read out using an EPR spectrometer. The specific spectrometer used was the Bruker EMX^{micro} spectrometer (X-band) which consists of a 9'' magnet. The spectrometer is also equipped with a highly sensitive resonator (ER4119HS-W1). Furthermore, the ambient temperature and humidity in the room were continuously monitored, of which the values are shown together in Table 5. It is also important that each alanine pellet is read out five times, each time at a different angle changing by 72°, after which an average of these five measurements is calculated. This ensures that there will be no angular dependency when calculating the final obtained absorbed dose of each pellet.

Table 5: Settings EPR spectrometer and environmental properties

Temperature (°C)	≈ 20
Humidity (%)	≤ 40
center magnetic field (mT)	348
sweep width (mT)	30
microwave power (mW)	0.25
field modulation (mT)	0.5
modulation frequency (kHz)	100
channels per sweep	2048
conversion time (ms)	40.96
sweep time (s)	83.89

The spectrometer will not continuously exhibit identical values of, for example, the field strength of the magnetic field. To correct for these variations, a reference was used. The reference in this case was chromium.

The irradiated alanine pellet is therefore read out at the same time as the reference, so that a correction can be made for any inconsistent temporal variation in the spectrometer sensitivity. Prior to reading out the pellets, they were each weighed separately from each other in order to correct the response for the variations in mass.

The peak-to-peak method is not used for the calculation of the dose. The effective dose calculations were performed with the amplitude method which uses the MATLAB code that was custom made by the primary standard lab of Physikalisch-Technische Bundesanstalt (PTB), located at Braunschweig, Germany.

For the uncertainty of the alanine dosimetry numerous parameters were taken into account (uncertainty on beam quality, environmental parameters, positioning, weighting,…). These are added in the results and should depict values around 1.0 %.

3.4.5 Dose verification using EBT3 gafchromic films

When designing the thorax phantom, the possibility of using EBT3 gafchromic films for dosimetry was also taken into account.

For this purpose, three locations were chosen where the films could be placed:

- completely through the phantom, thus also through the ribs and lungs (top film);
- at the back of the lungs adjacent to the ribs (middle film);
- through the spine (bottom film).

When manipulating the films it was always ensured that gloves were used. The films were stored in non-translucent storages.

It was always ensured that the films were placed touching the alanine pellets in order to be able to carry out dose verification using both methods and the radiotherapy dose plan.

The films were each cut into sizes that fit their corresponding place in the phantom, which were: 7 cm by 9.2 cm, 14.9 cm by 9.6 cm and 10.7 cm by 9.2 cm. An arrow was added on the top side in the left top corner of each film to have a mark for the correct orientation.

A distance of 6.65 cm functioned as buildup distance since the top film was placed at this distance. The source-to-film distance for the top film is 99.95 cm, for the middle film this is 102.7 cm and 103.6 for the bottom film. Each film was irradiated perpendicular to the 6 MV radiation beam.Templates were used (the size of the films was cut out of cardboard) so that the films had the same position, centered on the flatbed, thus avoiding lateral dependence effects. This is the process were the scanner lamp causes light scattering due to the particles in the active layer of the film which gives a nonuniform response of the readout.

As little light as possible protruded lateral to the films in each scan. The films were scanned in landscape mode with the short side parallel to the scan direction. The orientation of each film was marked with an arrow. Furthermore, a glass sheet was placed on top of the films and template, which caused compression and prevents the films from arching during scanning [28], [29].

The determination of the dose that the films have received is very different from the way in which the alanine pellets are read out. Before the films could be scanned, the flatbed scanner had to be heated by means of a fairly large number of 'empty' scans, which stabilized the scanner. The films, which consist of an active layer of approximately 0.028 mm with a matt polyester substrate layer of 0.12 mm thick on both sides, were scanned using an Epson expression 10000 XL scanner. The software that was used was included with the scanner (EPSON SCAN version 3.04). The scanner was used with following settings: 48-bit red green blue (RGB) mode, a resolution of 72 dpi and saved in tagged image file format (TIFF) format In order to calculate the dose FilmQA Pro was used, The values of the three color channels were used after the scan of the film was imported in the beforementioned software. Thereafter a comparison was made between the TPS dose plan and the data from the scanned films. The corresponding location of the film to the dose plan was determined using the dose matrix in 3D-slicer [28].

3.4.6 Clinic 1

The films were first read out 17 hours after irradiation. Eventually they were read twice more, after respectively 328 and 352 hours. In order to obtain an accurate reading of the dose when using the films, there must be a certain reference or comparability which can be achieved by calibrating the response of the film. This calibration of the film dose determination was not part of this study. It was performed at a previous date and time. Eight pieces of EBT3 film were irradiated using a 6 MV beam with a dose starting at 0.5 Gy and then doubling the dose per film up to 32 Gy in addition to the film with zero dose (no irradiation). For the irradiation of the films an SSD of 100 cm and a 10 by 10 cm^2 field was used with a nominal beam energy of 6 MV.

Hereafter the films were scanned and read out at several different times starting at 17 hours and ending at 352 hours each time with a 24 hour interval. The curve for the 17 hour post irradiation calibration is presented in Figure 16. For the other times of post irradiation when the films were scanned similar calibration curves were noticed so these were added to this thesis. From this curve it can be stated that the red channel and the green channel have a similar sensitivity when taking the first derivative. Since from experience the green channel presented the most accurate results, it will be used for calculation of the results in this thesis.

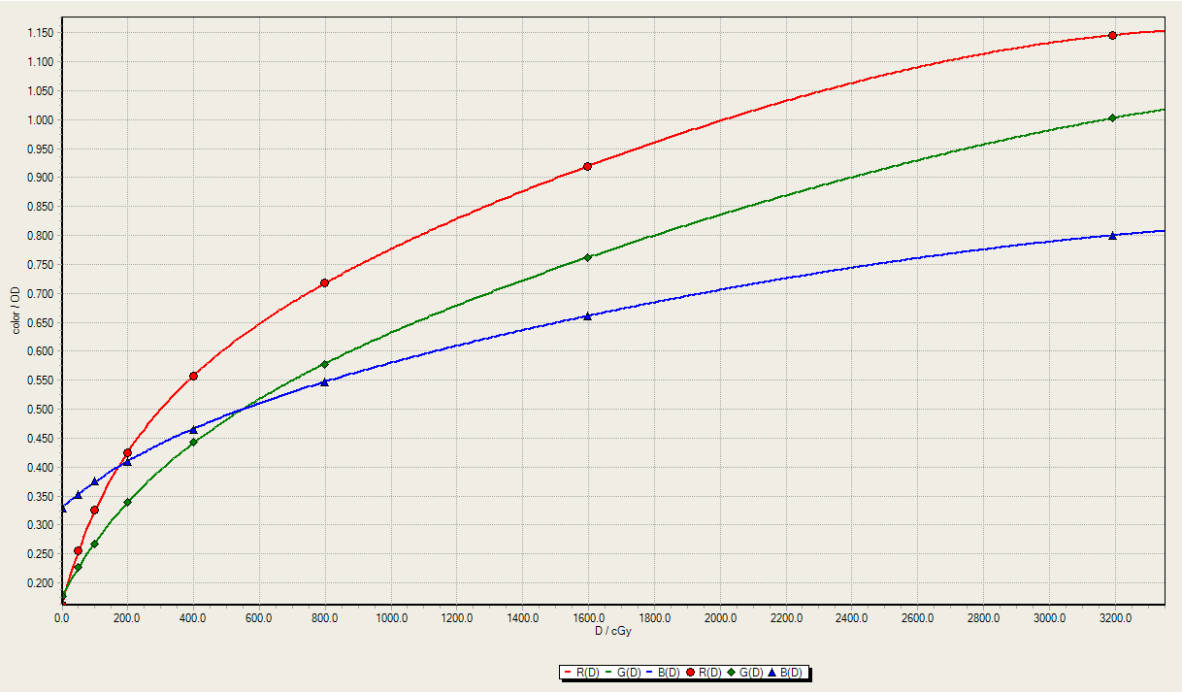

Figure 16: OD to dose calibration curve 17 hours after irradiation of the film

3.4.7 Clinic 2

For clinic 2 the same calibration curve was used but to limit the uncertainty on this curve the single scan method was utilized. Which means that aside from the irradiation of the phantom itself, a piece of film was irradiated in a small time frame using a beam energy of 6 MV, field size of 10 by 10 cm^2 and a set dose of 6 Gy with a SSD of 100 cm. Four alanine pellets were simultaneously irradiated at a depth of 1 cm PMMA, using a solid water slab phantom. Each film in the phantom was scanned together with the reference films irradiated with 6 Gy and one not irradiated, all from the same lot and with the same positioning. The calibration curve was then rescaled while utilizing the reference films and the mean dose readout of the four alanine pellets to acquire a more accurate readout.

The results of the EBT3 film dosimetry should be considered with an uncertainty of 1.5 % to 2.0 % and are measured by comparing the consistency maps to the dose maps. When combining alanine and EBT3 film dosimetry as done with the one-scan dosimetry for higher dose measurement accuracy, an estimation of the uncertainty is made by using following formula:

$$\sqrt{(U_1)^2 + (U_2)^2} = U_T \quad (3)$$

With U_1 representing the uncertainty of the alanine dosimetry and U_2 representing the uncertainty of the EBT3 film dosimetry equaling to U_T which depicts the total uncertainty of the combined dosimetry system. When calculated using the respective values, a minimal total uncertainty of 1.80 % to 2.24 % should be considered.

4 Results

4.1 3D-printed phantom

First, the results concerning the design of the thoracic phantom using Autodesk Fusion 360 are set out step by step. This includes the addition of areas to fit the dosimeters used for the final dosimetry. Second, the design of the rib and spine molds is shown and lastly the resulting 3D-printed phantom is exhibited.

4.1.1 Design

Figure 17 shows the 2D representation which is identical for the front and the back of the thoracic phantom with the delineation of the lungs and the spine. The body of soft tissue was depicted as an oval with one side cut off in such a way that the phantom can be placed on the table in a stable way.

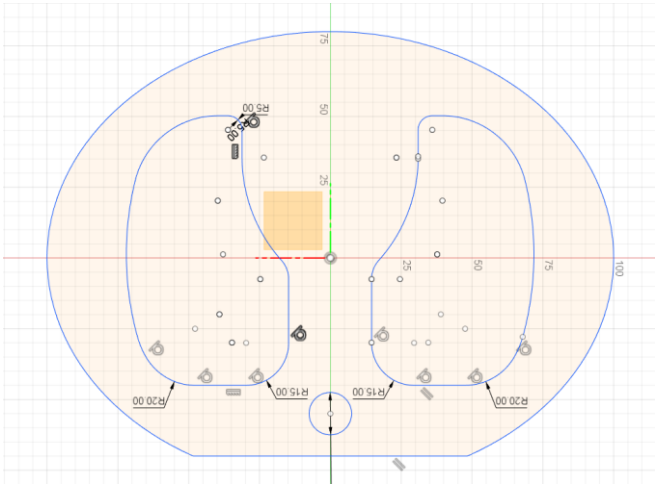

Figure 17: 2D-representation front side thoracic phantom

As represented in Figure 18 and Figure 19, it was decided to model one rib along one side of the phantom, i.e. along one lung, and to mirror this alongside the depth axis seven times. Then the entire volume was mirrored along the inside plane, creating a 3D-representation of a whole phantom with two lungs and one spine left out.

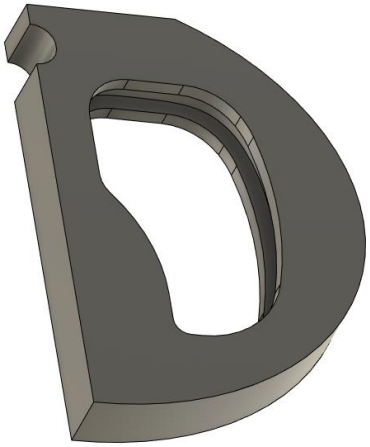

Figure 18: Designing of a 3D-volume for the thorax phantom showing the design of one rib on one side

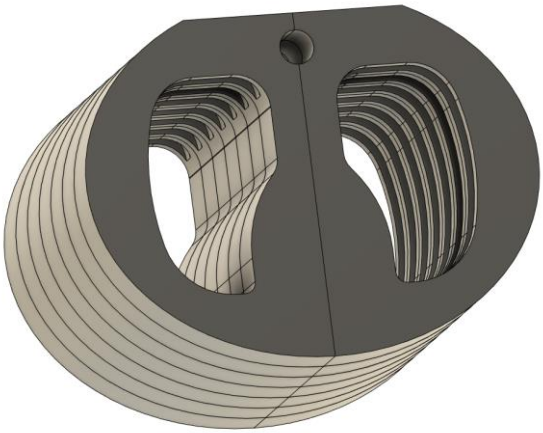

Figure 19: Designing of a 3D-volume for the thorax phantom depicting the full volume containing 7 ribs on each side

4.1.1.1 Dosimeter fitting

Figure 20 shows the division of the phantom where the positions of the films, all three adjacent to the alanine pellets, are indicated. Inserts were designed for a total of 14 alanine pellets and room for 3 films. Space was thus left to place films through the entire phantom, including the lungs (red + blue line), adjacent to the ribs (green line) and through the spine (yellow line). Figure 21 represents the split lung insert with addition of the location of the film.

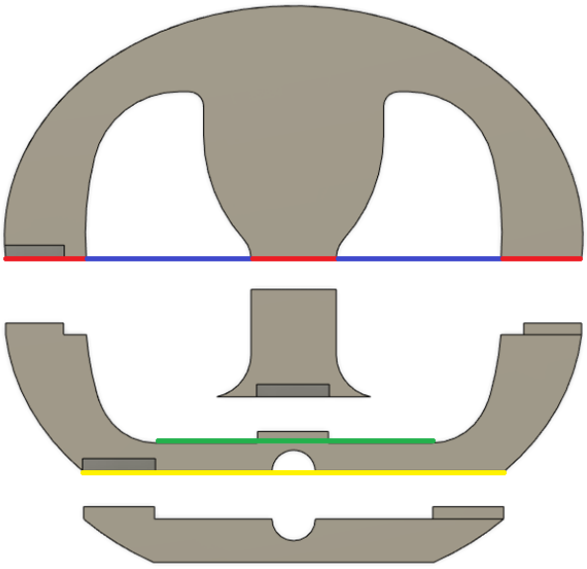

Figure 20: Front view of the different segments including different color lines to depict the designated film locations

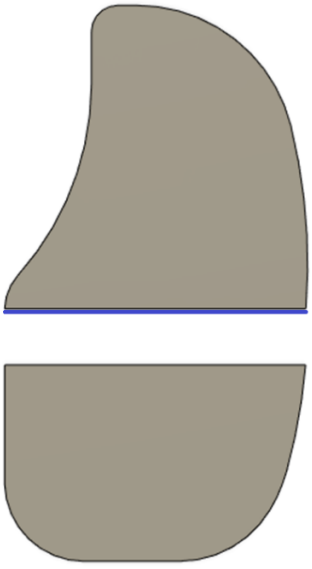

Figure 21: Front view of the lungs

Nine of the total of fourteen designed alanine inserts are visible in Figure 22. In addition, three more can be found in the lungs themselves depicted in Figure 23 and Figure 24.

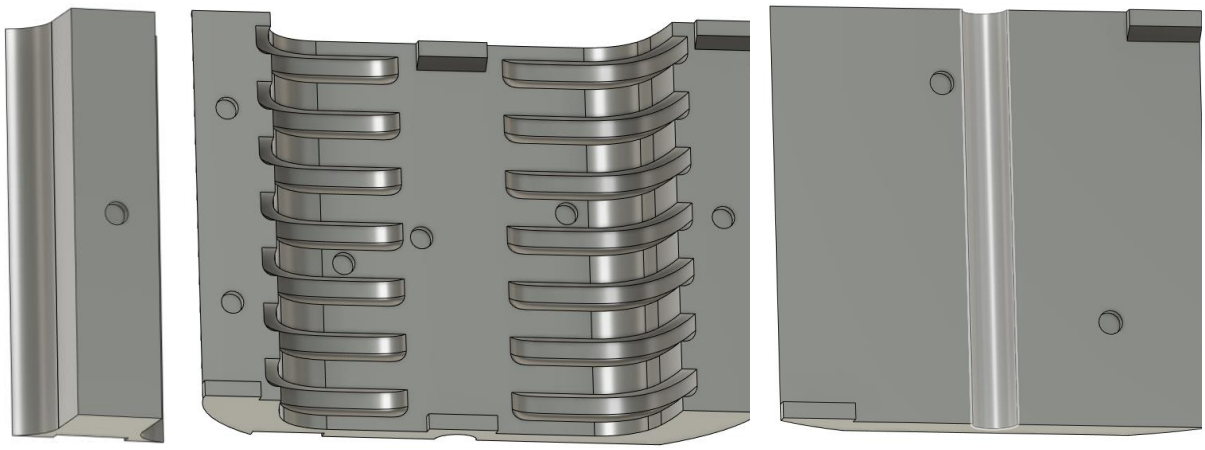

Figure 22: Visualization of 9 of the total of 14 alanine cutouts in 3 different segments of the thoracic phantom

Figure 23: Design of two part left lung containing 2 alanine inserts

Figure 24: Design of two part right lung containing 1 alanine insert

4.1.1.2 Spine and rib molds

Depicted in Figure 25 and Figure 26 are the designs of the molds for the front part of the spine and for one right rib respectfully. To design these, the spine molds were modeled in two parts of which one part had a lid with two circular protrusions with dimensions slightly larger than those of an actual alanine pellet. As a result of this, the silicone cures with two inserts to snugly fit one alanine pellet each. The rib molds were designed in two pieces so no cutting of the cured silicone had to be performed.

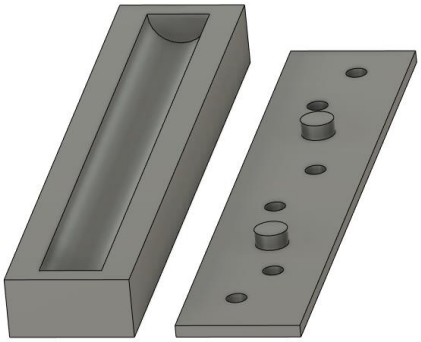

Figure 25: Spine mold with lid

Figure 26: Mold for right rib

4.1.2 3D-printing

All parts of the resulting 3D-printed thoracic phantom are shown in Figure 27, the ribs are already fitted in place. Figure 28 visualizes the dimensions of the total phantom having a width of 150 mm, a height of 112.5 mm and a length of 105 mm. Important to mention is that protrusions were also provided at the top and bottom of the phantom to ensure more solidity between the various parts. It was important to take into account the sturdiness during the printing process of the protrusions at the top. During printing, the filament does not harden immediately, which can cause it to sag if no reinforcement is provided underneath. This resulted in the design of a slope of 45° instead of using a square corner of 90°, which gradually increased the pressure and provides enough strength to prevent the molten filament from sinking, this is visualized in Figure 29.

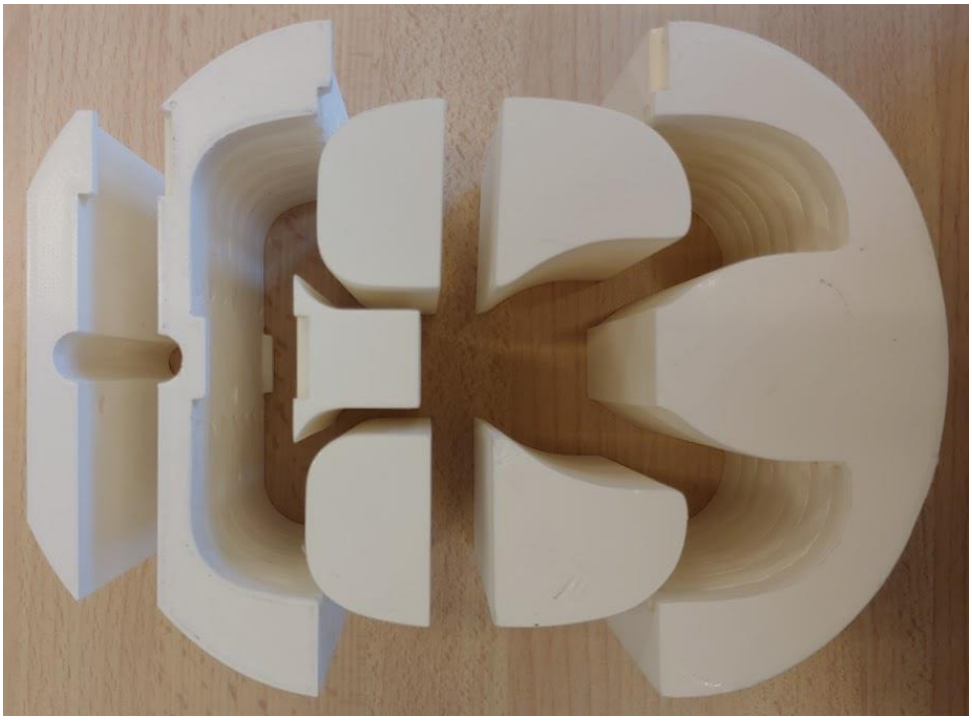

Figure 27: All segments of 3D-printed thoracic phantom with rib inserts fitted in place

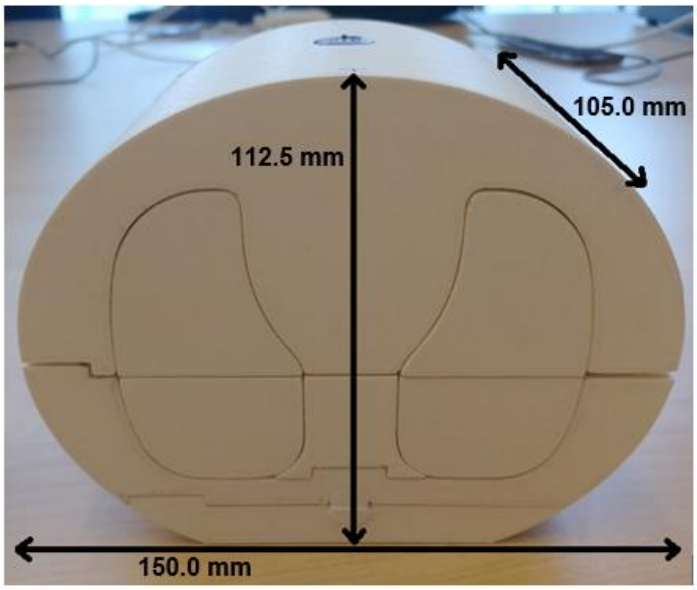

Figure 28: Finalized 3D-printed thoracic phantom presented with its dimensions

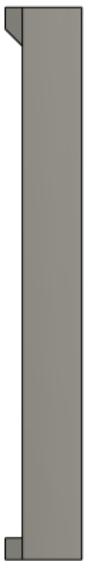

Figure 29: Side view of the rear segment design with an angled protrusion

Since the lungs were printed with the same dimensions as the orifices in the phantom itself, there were issues with the fitting even after a significant amount of sanding. This can be noticed on Figure 28 by the gap on both the left and right lateral side of the phantom neighboring the lungs.

4.2 Bone equivalent material

4.2.1 Imaging properties

First, the homogeneity of silicone type 1 and silicone type 2 were visually reviewed in order to decide on which silicone to continue this study with. The relation of the amount of $CaCO_3$ added to the silicone to the HU that are reached on a CT-scan was subsequently determined, This was done by choosing a selection of regions of interest throughout each sample and calculating the mean HU, which is accompanied with a standard deviation (SD). These results can be found in Table 6 and afterwards they are graphically plotted.

Figure 30 and Figure 31 display CT-scans of silicone type 1 and silicone type 2 respectively. Both mixed with an unmeasured amount of $CaCO_3$. Figure 30 shows that the $CaCO_3$ in the silicone type 1 is sunken to the bottom resulting in no homogeneity throughout the sample. Figure 31 shows a great homogeneity of the $CaCO_3$ throughout the entire sample with the presence of air pockets. Because of the homogeneity viewable on the CT-scan with silicone type 2, it was decided to continue the rest of this thesis with that type of silicone.

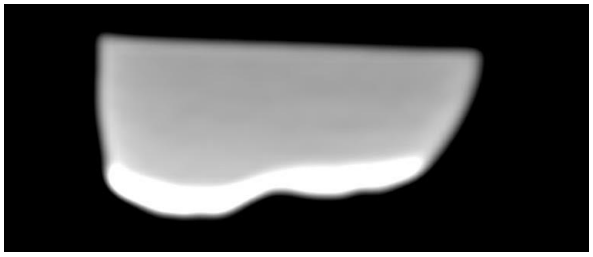

Figure 30: CT-image showing silicone type 1 with the sunken $CaCO_3$

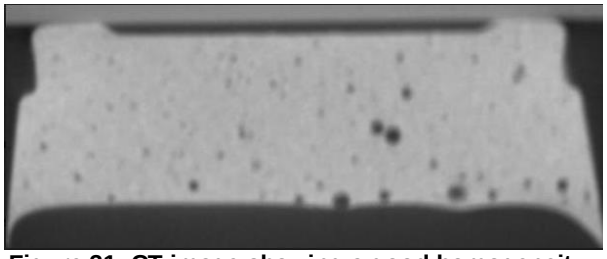

Figure 31: CT-image showing a good homogeneity of the $CaCO_3$ throughout the sample of silicone type 2

Table 6 shows the HU measured of ten samples of silicone using various ROI throughout the samples with addition of the SD on the mean value of HU. Each sample contained an increasing amount of $CaCO_3$ starting with 3.01 g ranging to 16.04 when 10 ml of silicone was used. The results show an increase in HU when the amount of $CaCO_3$ is increased. When doubling the amount of base and catalyst, still utilizing the 1 to 1 mixing ratio, to a total of 20 ml of silicone no change of results is visible.

Table 6: HU in relation to the amount of $CaCO_3$ added to the silicone

amount of silicone (ml)	10									20
amount of CaCO3 (g)	3.01	4.04	5.01	6.02	7.93	10.01	12.02	14.03	16.04	20.06
min HU	410	493	533	648	703	818	760	748	873	707
max HU	566	695	754	892	1052	1134	1197	1268	1346	1161
mean HU	449.66	550.13	603.51	740.47	895.56	964.09	992.82	1043.1	1178.32	919.81
SD on mean HU	23.36	39.12	52.17	47.79	60.59	70.22	62.7	55.58	59.92	66.26

Figure 32 depicts the minimum, maximum and mean HU that were measured of each sample plotted to the increasing amount of $CaCO_3$ added. For the minimum values a logarithmic curve can be plotted: $y = 257.71\ln(x) + 144.48$ with an R^2 value of 0.9153. For the maximum values the logarithmic curve would be $y = 470.71\ln(x) + 38.415$ with an R^2 value of 0.9934. For the mean values this results in the curve: $y = 424.64\ln(x) - 33.673$ with an R^2 value of 0.9808.

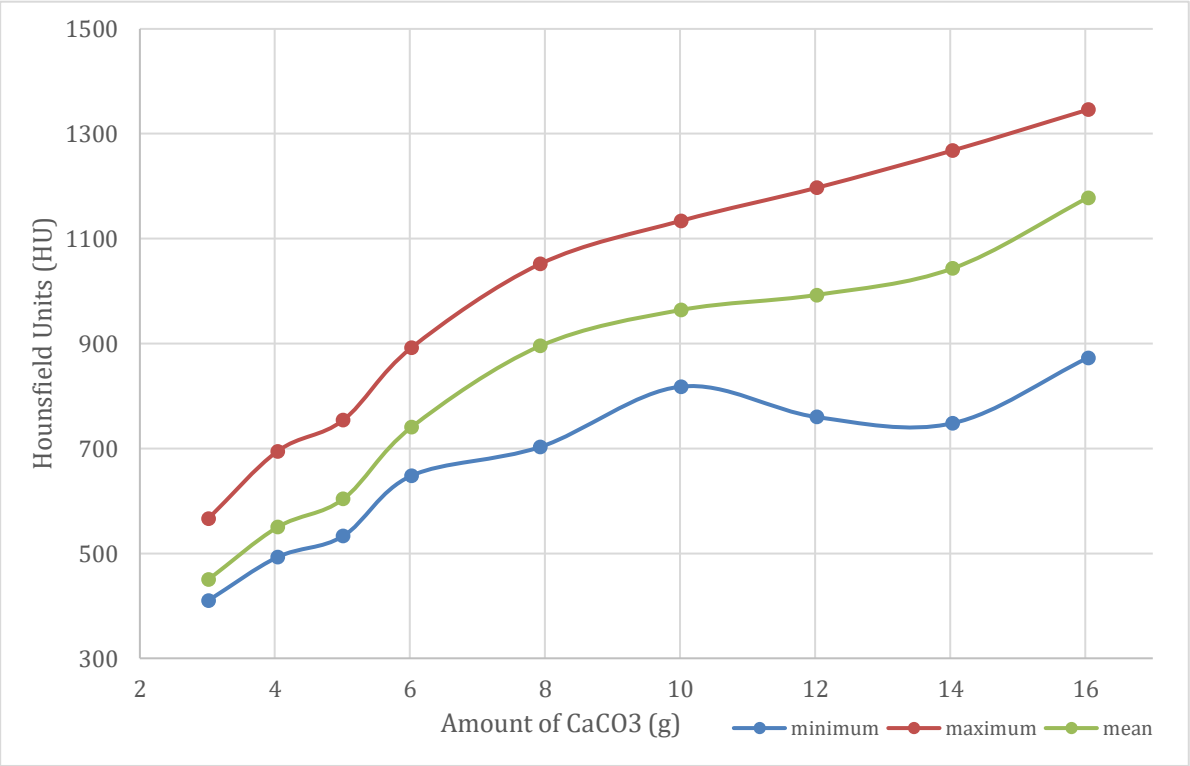

Figure 32: Minimum, maximum and mean HU for each silicone sample plotted in relation to the amount of $CaCO_3$

Table 7 shows the amount of $CaCO_3$ needed to mimic the ribs and spine according to the HU using interpolation of the mean values found in Table 6. For the fabrication of the final ribs and front of the spine an amount of 3 grams of $CaCO_3$ was used. The back of the spine shall consist of 5 grams.

Table 7:Amount of $CaCO_3$ to mimic Human ribs and spine

	HU	CaCO3 needed (g)
human ribs	400 - 550	2.78 - 3.95
human spine (front)	400 - 550	2.78 - 3.95
human spine (back)	550 - 700	3.95 - 5.63

4.2.2 Silicone density

The measured density of the silicone mixed with 9 grams (to represent ribs and the front of the spine) and 15 grams (to represent the back of the spine) of $CaCO_3$ is set out in Table 8. When compared to the densities proposed by the Eclipse TPS depicted in Table 10, an overestimation is made by the TPS for all bone equivalent segments.

Table 8: Calculated density of the silicone and $CaCO_3$ mixture

CaCO3 (g)	9	15
Total volume mixture (ml)	30	30
Total weight mixture (g)	37.0	40.7
Density mixture (g/ml)	1.23	1.36

4.3 Imaging verification of thoracic phantom

4.3.1 Soft, lung and bone tissue

Figure 33 depicts a CT-scan of the finalized phantom. The 3D-printed infill structures and densities are clearly visible, showing more air in the lungs. Four of the fourteen alanine pellets and the bone equivalent material are also visible in this particular scan. The mean HU of several ROI are shown in Table 9 and in correlation to the numbers of the different parts shown in Figure 33 together with the desired amount of HU to resemble the correct tissue. This was done for soft, lung and bone tissue.

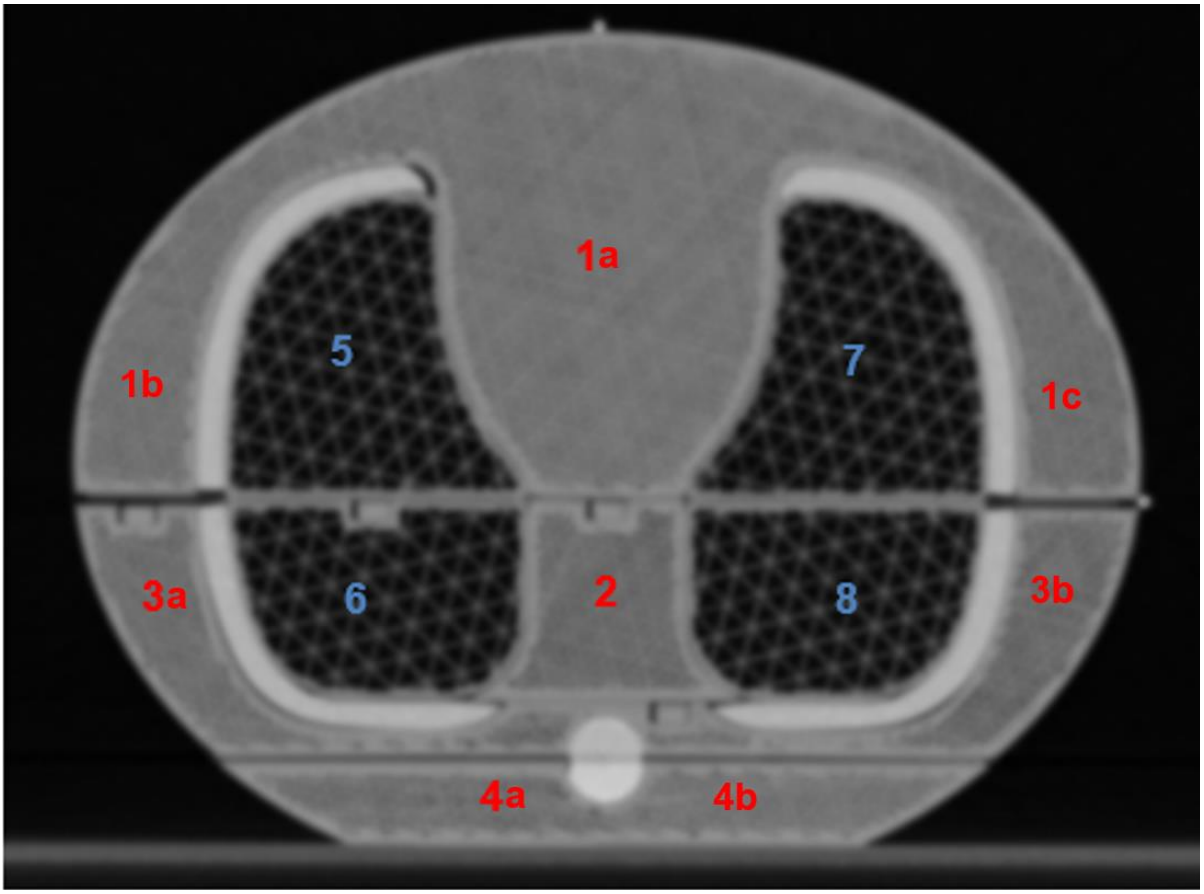

Figure 33: CT-scan finalized 3D-printed thoracic phantom containing bone equivalent material for ribs and spine. 4 alanine pellets are also shown

Table 9 shows the results of the measured HU with corresponding SD using various ROI throughout the phantom. For both soft and lung tissue the measured CT-values are lower than the reference values. The standard deviation for the lungs proof more than 100 for all four segments. It is also noticeable that variations in the same segment are present. The most significant one is between segment 1b and 1c, an absolute difference of 36.1 HU is present which equals to a relative difference of 61.9 %. The measured values for the bone equivalent material conform to the reference values.

Table 9: Measured mean Hounsfield Units and corresponding standard deviation for the different segments of the 3D-printed lung soft tissue, ribs and spine compared to the reference Hounsfield Units of the respectable tissue

	Reference CT-values (HU)	Segment	Mean measured CT-values (HU)	SD
Soft tissue	0	1a	-59.52	23.28
		1b	-58.32	17.14
		1c	-94.42	21.61
		2	-132.45	27.5
		3a	-101.02	19.06
		3b	-116.30	24.92
		4a	-75.92	29.81
		4b	-106.81	31.05
Lung tissue	-700 to -600	5	-777.45	110.13
		6	-773.36	109.93
		7	-782.52	109.32
		8	-767.26	115.59
Ribs + front spine	400 to 550	/	482.72	12.49
Back spine	550 to 700	/	695.42	11.56

Table 10 depicts the values of several properties calculated by the TPS using AXB$_M$ at clinic 2. In comparison to Table 9 the results show similar variations to the CT-values for the soft tissue. The average CT-value for the lungs shows a better representation to the theoretical value. For the bone material we see a lower estimation of the CT-values.

Table 10: Depiction of several properties concerning all different materials in the 3D-printed phantom calculated by the TPS in clinic 2

	back spine	Front spine	ribs	lungs (average)	best case soft tissue	worst case soft tissue
CT-value (HU)	603	419	429	-710	-36	-115
Mass density (g/cm3)	1.449	1.33	1.335	0.289	0.993	0.908
Relative electron density	1.378	1.276	1.28	0.282	0.983	0.933
Proposed physical material composition	30 % cartillage	54 % cartillage	53 % cartillage	100 % lung	24 % adipose tissue	100 % adipose tissue
	70 % bone	48 % bone	47 % bone		76 % muscle skeletal	

4.4 Dosimetry verification of thoracic phantom clinic 1

For the results of the film dosimetry at clinic 1 utilizing the standard calibration curves, only the horizontal dose profiles are presented. No additional useful information could be retrieved form the vertical dose profiles and were thus not added to this thesis.

4.4.1 Film dose readout after 17 hours

Figure 34 depicts the dose profiles for the calculated dose plan by the TPS using AXB$_M$ compared to the film dose of the film located at the top position in the thoracic phantom, through the lungs. The dose profiles show the width of the used irradiation field of 10 cm. A similar shaped curve can be noticed with an underestimation of the dose given by the TPS. The mean dose difference has a relative value of 7.8 % with a max difference of 30.1 % towards the edges of the dose profile.

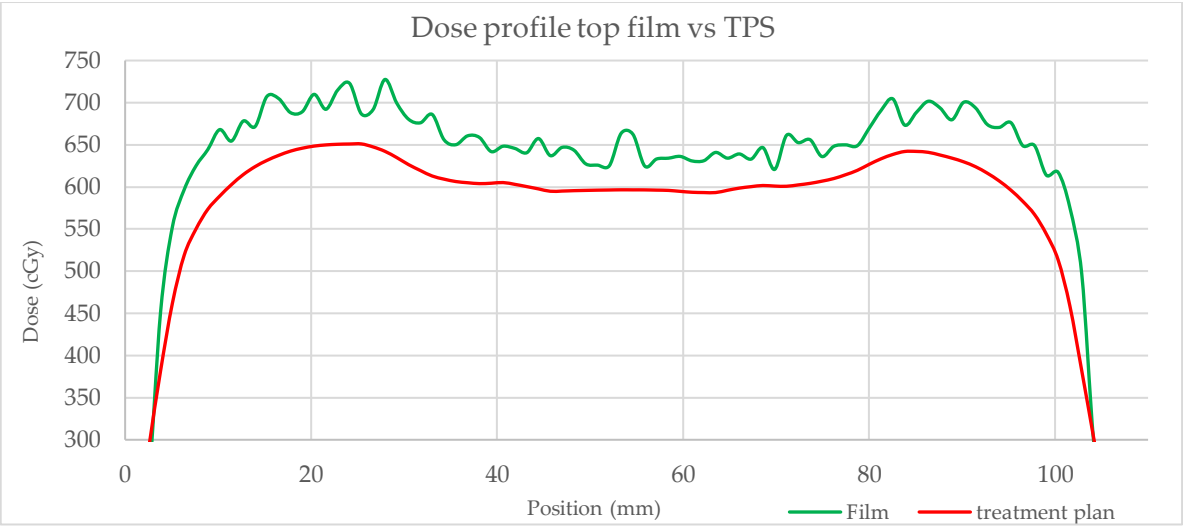

Figure 34: Dose profile comparison for the dose calculated by the TPS (AXB$_M$) and the measured top film dose according to the calibration curve for 17h after irradiation

Figure 35 presents the dose profiles for the calculated dose plan by the TPS using AXB$_M$ compared to the film dose of the film located at the middle position in the phantom at the position where the lung tissue ends and soft tissue/bone tissue (ribs) start. The dose profiles show a film width of approximately 8 cm which complicated the alignment of the film profile to the TPS dose profile. A significant dose difference can be noted at the position of the lungs, especially the right lung. A mean relative difference of 11.4 % is present.

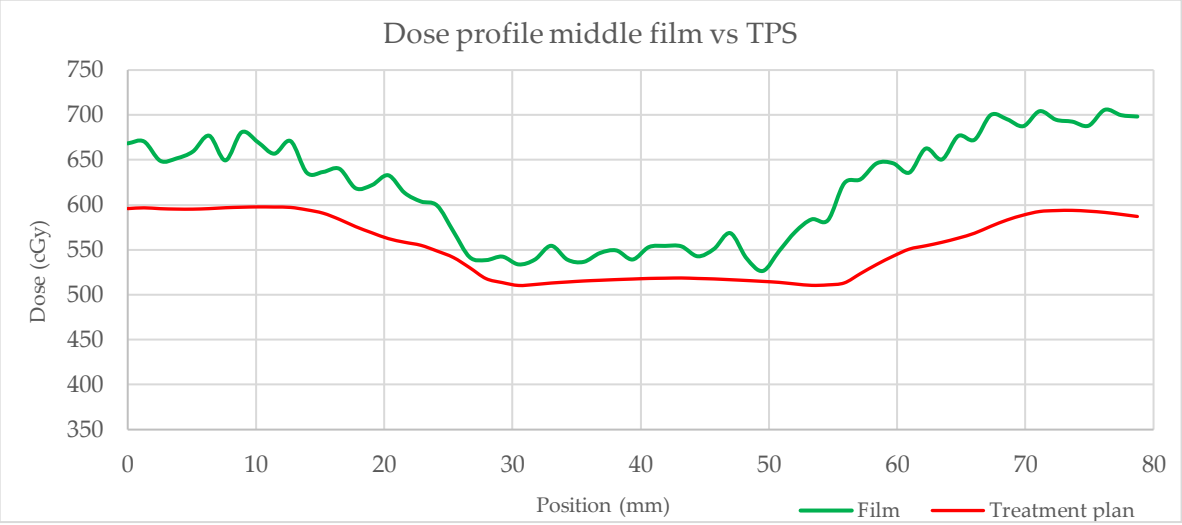

Figure 35: Dose profile comparison for the dose calculated by the TPS (AXB$_M$) and the measured middle film dose according to the calibration curve for 17h after irradiation

Figure 36 displays the dose profiles for the calculated dose plan by the TPS using AXB$_M$ compared to the film dose of the film located at the bottom position in the phantom through the spine and at the position where the ribs end. A similar dose profile as with the top film can be noted with a significant underestimation of the dose by the TPS and a mean and max dose difference of respectively 13.1 % and 38.4 % towards the edges of the dose profile.

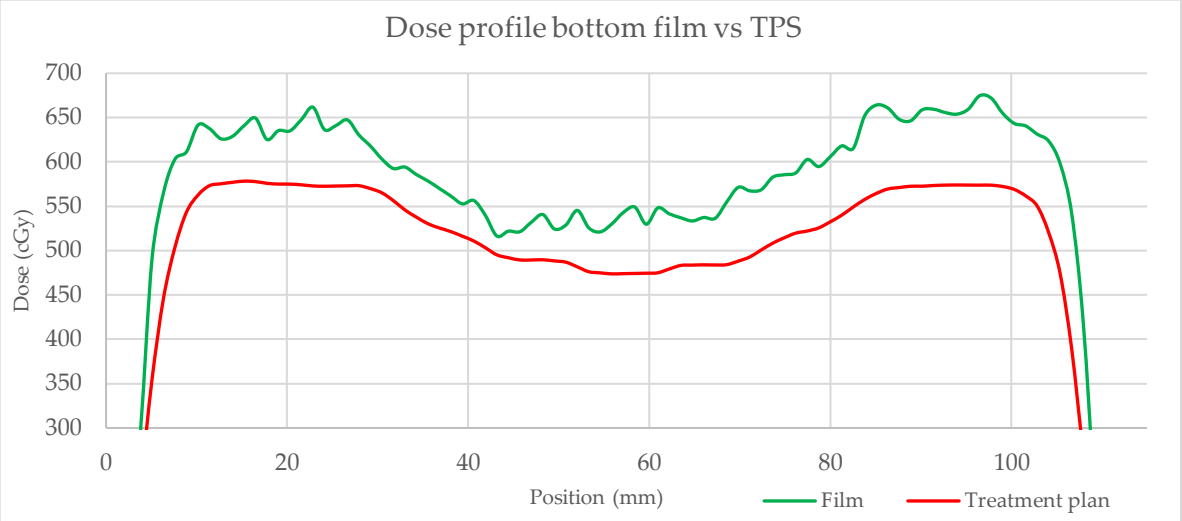

Figure 36: Dose profile comparison for the dose calculated by the TPS (AXB_M) and the measured bottom film dose according to the calibration curve for 17h after irradiation

4.4.2 Film dose readout after 328 hours

Figure 37 represents the dose profiles for the calculated dose plan by the TPS using AXB_M compared to the film dose of the film located at the top position in the phantom, through the lungs. The dose profiles show a similar shaped curve with an underestimation of the dose given by the TPS. The mean dose difference has a relative value of 14.7 % with a max difference of 60.9 % towards the edges of the dose profile.

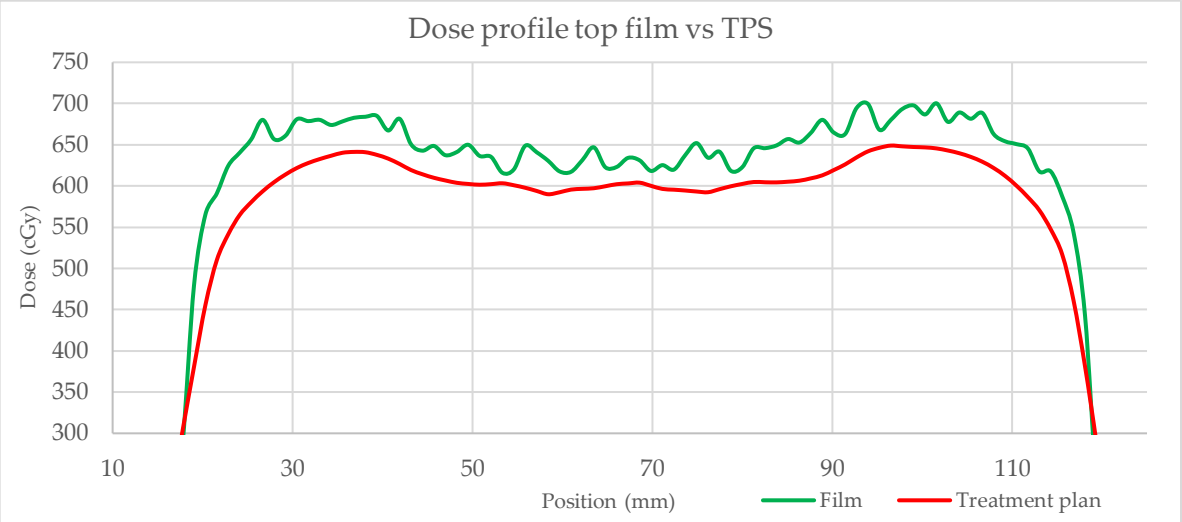

Figure 37: Dose profile comparison for the dose calculated by the TPS (AXB_M) and the measured top film dose according to the calibration curve for 328h after irradiation

Figure 38 depicts the dose profiles for the calculated dose plan by the TPS using AXBM compared to the film dose of the film located at the middle position in the phantom at the position where the lung tissue ends and soft tissue/bone tissue (ribs) start. The dose profiles show a film width of approximately 8 cm which complicated the alignment of the film profile to the TPS dose profile. A significant dose difference can be noted at the position of the lungs, especially the left lung. A max relative difference of 18.3 % and a mean difference of 9.2 % are present.

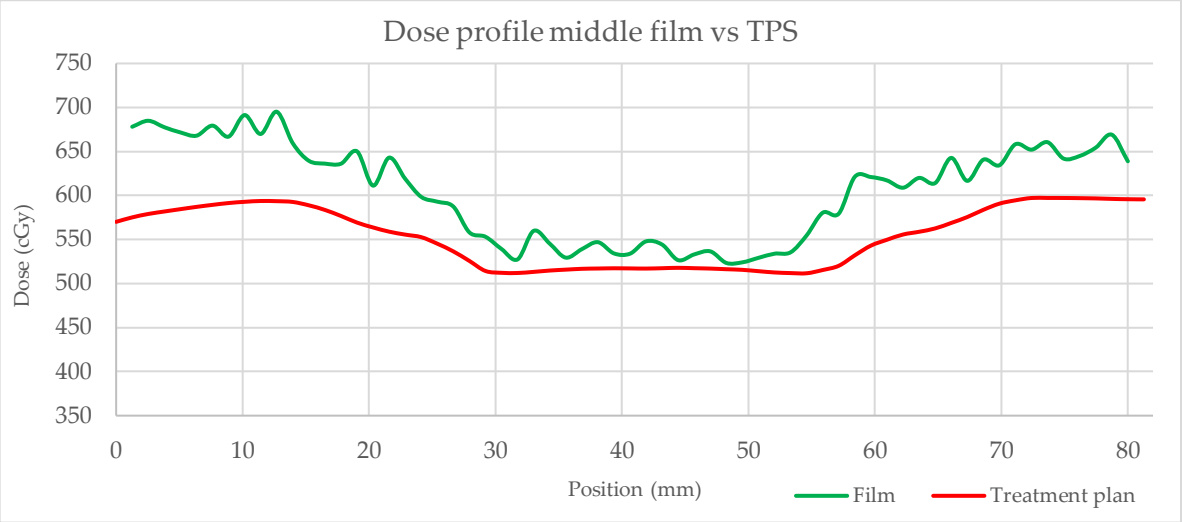

Figure 38: Dose profile comparison for the dose calculated by the TPS (AXBM) and the measured middle film dose according to the calibration curve for 328h after irradiation

Figure 39 displays the dose profiles for the calculated dose plan by the TPS using AXBM compared to the film dose of the film located at the bottom position in the phantom through the spine and at the position where the ribs end. An underestimation of the dose by the TPS and a mean and max dose difference of respectively 8.7 %and 53.8 % can be noted. Between 60 and 80 mm a less significant underestimation can be determined with a mean difference of 3.5 %.

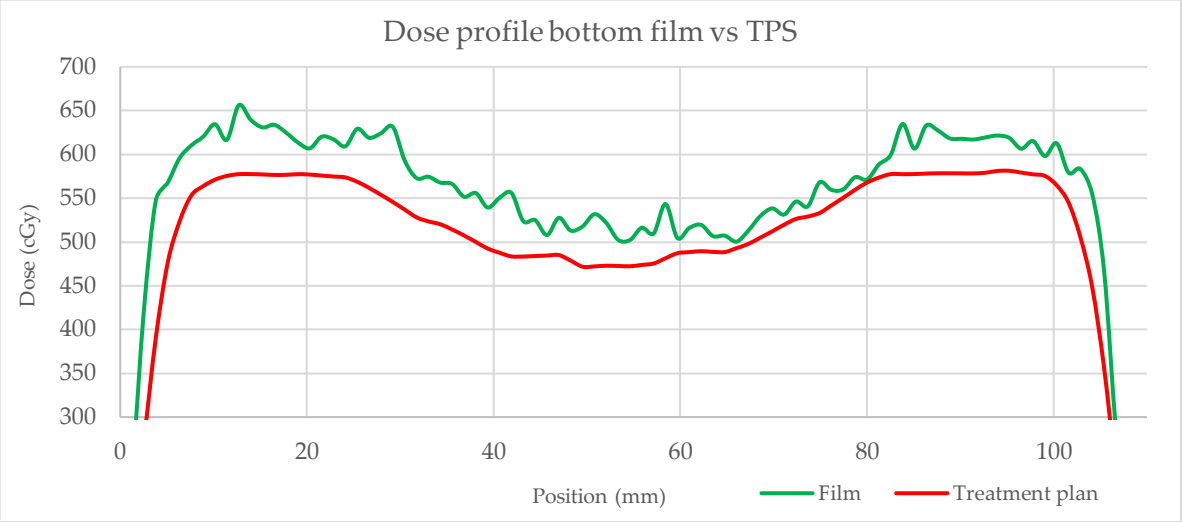

Figure 39: Dose profile comparison for the dose calculated by the TPS (AXB$_M$) and the measured bottom film dose according to the calibration curve for 328h after irradiation

4.4.3 Film dose readout after 352 hours

Figure 40 depicts the dose profiles for the calculated dose plan by the TPS using AXB$_M$ compared to the film dose of the film located at the top position in the phantom, through the lungs. The dose profiles show a similar shaped curve with an underestimation of the dose given by the TPS. The mean dose difference has a relative value of 17.3 % with a max difference of 63.8 % towards the edges of the dose profile.

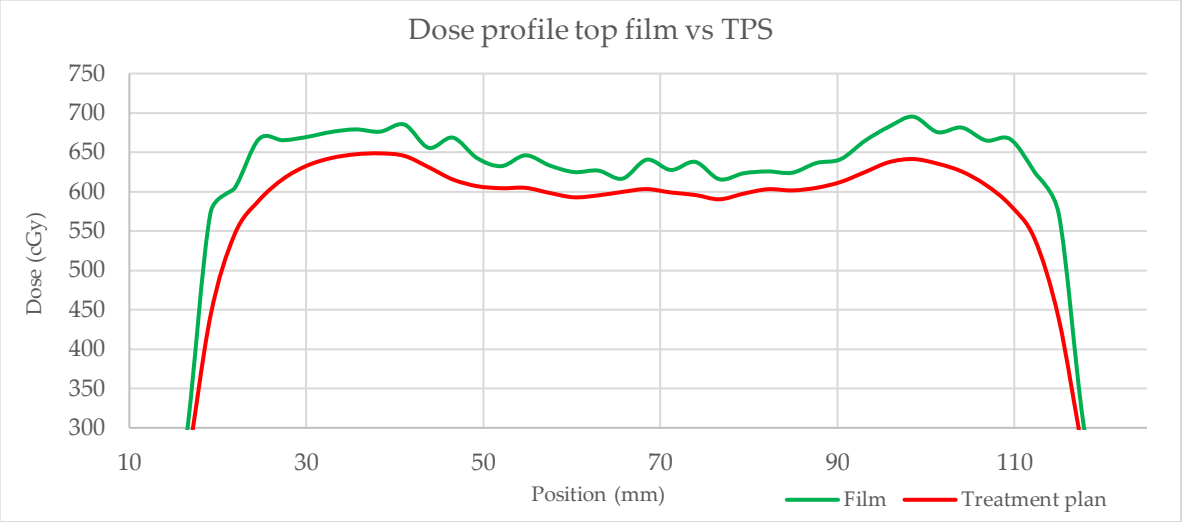

Figure 40: Dose profile comparison for the dose calculated by the TPS (AXB$_M$) and the measured top film dose according to the calibration curve for 352h after irradiation

Figure 41 represents the dose profiles for the calculated dose plan by the TPS using AXB$_M$ compared to the film dose of the film located at the middle position in the phantom at the position where the lung tissue ends and soft tissue/bone tissue (ribs) start. The dose profiles show a film width of approximately 8 cm which complicated the alignment of the film profile to the TPS dose profile.

A dose difference can be noted throughout but especially in the right lung. A max relative difference of 19.1 % and a mean difference of 8.0 % are present with a mean difference of 12.5 % for the positions from 55 to 80 mm in comparison to a mean dose difference of 5.8 % for the region of 5 to 30 mm.

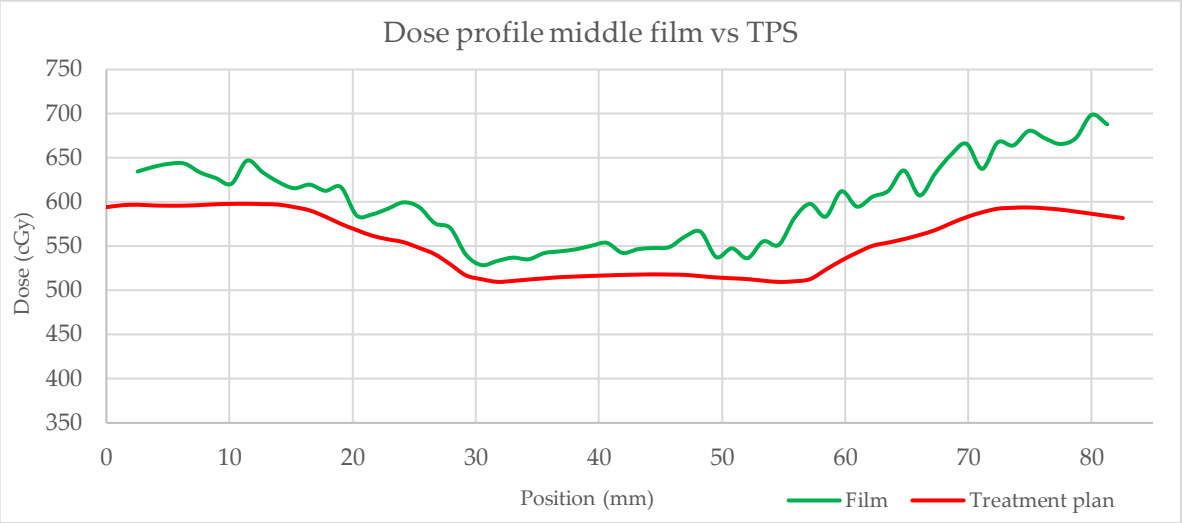

Figure 41: Dose profile comparison for the dose calculated by the TPS (AXB$_M$) and the measured middle film dose according to the calibration curve for 352h after irradiation

Figure 42 displays the dose profiles for the calculated dose plan by the TPS using AXB$_M$ compared to the film dose of the film located at the bottom position in the phantom through the spine and at the position where the ribs end. An underestimation of the dose by the TPS and a mean and max dose difference of respectively 12.4 % and 47.9 % can be noted. Between 25 and 45 mm, a less significant underestimation can be determined with a mean difference of 5.2 %.

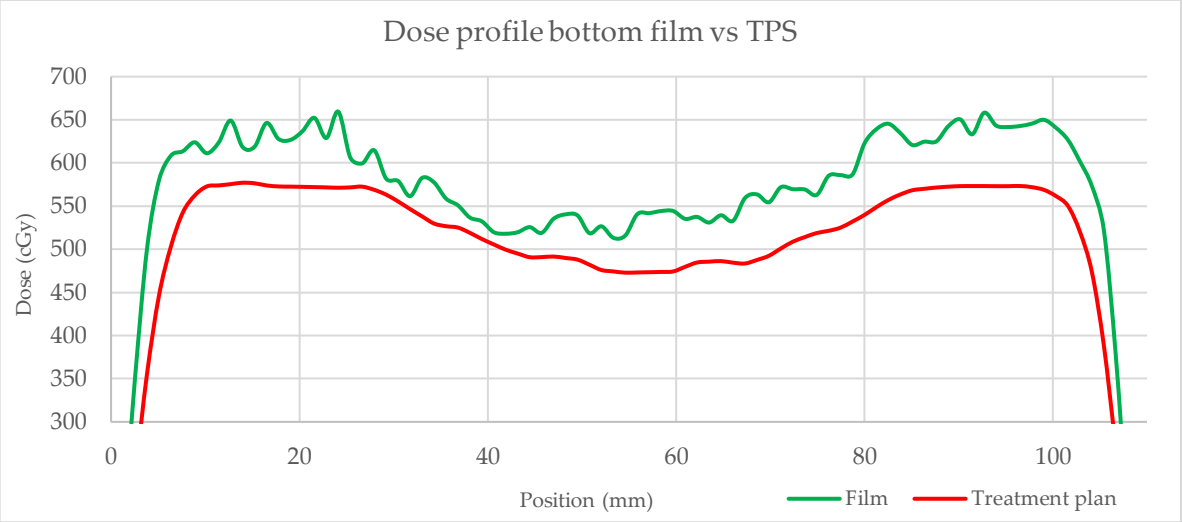

Figure 42: Dose profile comparison for the dose calculated by the TPS (AXB$_M$) and the measured bottom film dose according to the calibration curve for 352h after irradiation

4.4.4 Alanine

Fourteen alanine pellets were fitted inside the phantom to measure the dose alongside the gafchromic EBT3 film. NS-control, NS-control 1 and 5 were located in the lungs touching the top film, NS-control 10 and 11 were located in the front part of the spine equivalent material. The rest of the pellets were found in the soft tissue equivalent material with NS-control 2, 3 and 6 located outside of the 10 x 10 cm irradiation field. The results depicted in Table 11 and Figure 43 show that the relative difference between the absorbed dose calculated by the TPS using AXB_M and the measured dose does not exceed 3.4 percent with exceptions of NS-control 3 located outside the irradiation field. With such low doses for alanine, the uncertainty of the pellets located outside the irradiation field depict values conforming to the dose differences compared to the TPS.

Table 11: The mean absorbed dose calculated by the TPS, compared to the mean measured dose of the alanine with the absolute and relative difference and the location of the alanine pellets related to the film regions

		Absorbed dose				
Film region	Alanine pellet	TPS (Gy)	measured (Gy)	Absolute difference (Gy)	Relative difference (%)	uncertainty (%)
Top film	NS-control	6.352	6.456	0.104	1.63	1.09
	NS-control 1	6.304	6.507	0.204	3.23	1.09
	NS-control 2	0.212	0.218	0.007	3.23	22.92
	NS-control 3	0.212	0.262	0.050	23.36	19.13
	NS-control 4	5.835	5.934	0.099	1.70	1.14
	NS-control 5	6.413	6.520	0.107	1.66	1.08
	NS-control 6	0.259	0.268	0.009	3.38	18.68
Middle film	NS-control 7	6.021	5.910	-0.110	-1.84	1.14
	NS-control 8	4.980	5.045	0.065	1.30	1.25
	NS-control 9	6.014	6.046	0.032	0.52	1.13
Bottom film	NS-control 10	4.846	4.928	0.082	1.70	1.27
	NS-control 11	4.842	4.914	0.072	1.48	1.22
	NS-control 12	5.680	5.659	-0.020	-0.36	1.17
	NS-control 13	4.717	4.758	0.041	0.88	1.25

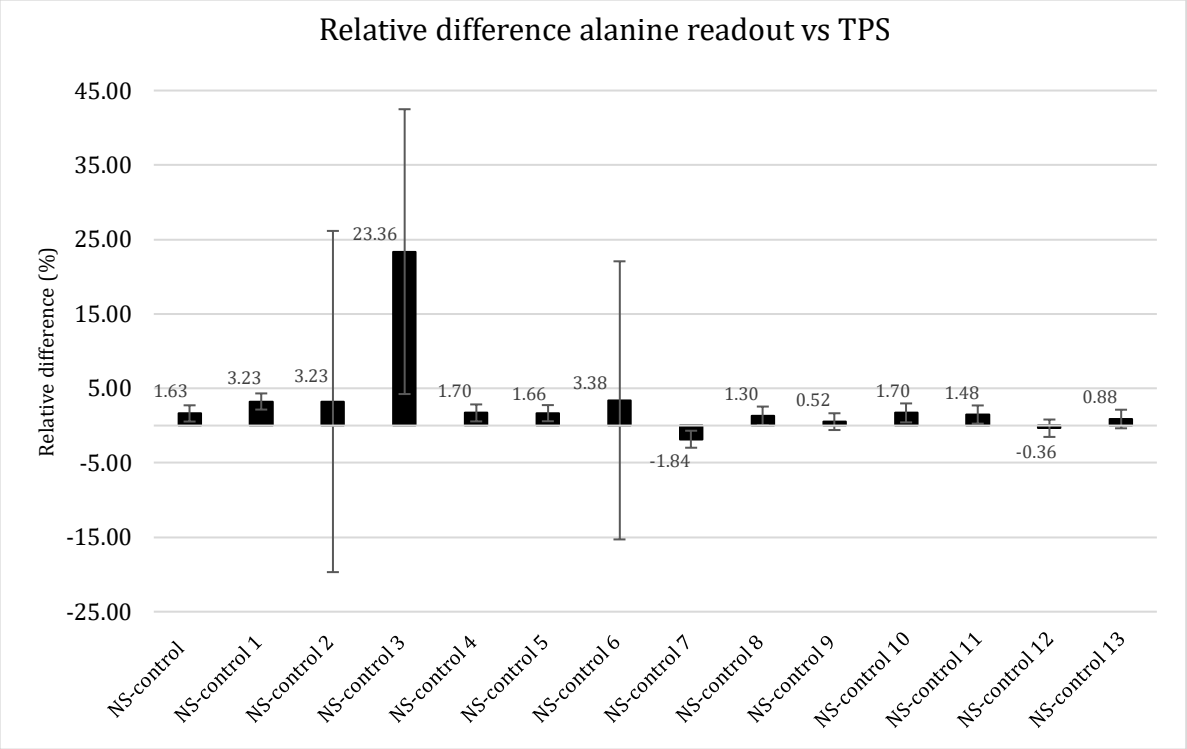

Figure 43: Relative difference between the alanine measurement and the dose calculated by the TPS for all alanine pellets: NS-control to NS-control 13

4.4.5 Total dose results comparison

The data for the films read out after 328 hours after irradiation was mirrored since most likely the films were scanned wrong side up causing the left side to be the right side of the dose profile compared to the TPS data.

Figure 44 depicts the comparison of the dose of the alanine pellets at the top film region (in the lungs) in the phantom with the exception of the pellets placed outside of the irradiation field (NS-control 2, 3 and 6) and the respective film read out at 17, 328 and 352 hours after irradiation to the dose calculated by the TPS using AXBM. The alanine pellets show a more acceptable deviation with a max difference of 3.2 %. Regarding the film, a significant difference of maximum 11.4 % and minimum 5.6 % is visible. It can be noted that the more time passes after irradiating, the more the dose drops except for NS-control 1.

Figure 45 represents the comparison of the dose of the alanine pellets at the middle film region (transition from lungs to ribs and soft tissue) in the phantom and the respective film read out at 17, 328 and 352 hours after irradiation to the dose calculated by the TPS using AXBM. The alanine pellets show a more acceptable deviation with a max difference of -1.8 %. Regarding the film, a significant difference of maximum 15.5 % and minimum 5.5 % is visible. It can be noted that the more time passes after irradiating, the more the dose drops.

Figure 46 visualizes the comparison of the dose of the alanine pellets at the bottom film region (through and on each side of the spine) in the phantom and the respective film read out at 17, 328 and 352 hours after irradiation to the dose calculated by the TPS using AXBM. The alanine pellets show a more acceptable deviation with a max difference of 1.7 %.

Regarding the film, a significant difference of maximum 15.1 % and minimum 8.1 % is visible. Only for NS-control 13 It can be noted that the more time passes after irradiating, the more the dose drops. NS-control 10 and 11 were positioned in the spine and show a lower deviation when read out after 328 hours compared to 352 hours. For the alanine the deviation by the dose measurement is similar (1.7 % and 1.5 % respectively).

Since all results in clinic 1 regarding EBT3 film dosimetry depict a systematic overestimation of the dose by the films gives a valid reason to re-irradiate the phantom using one-scan dosimetry.

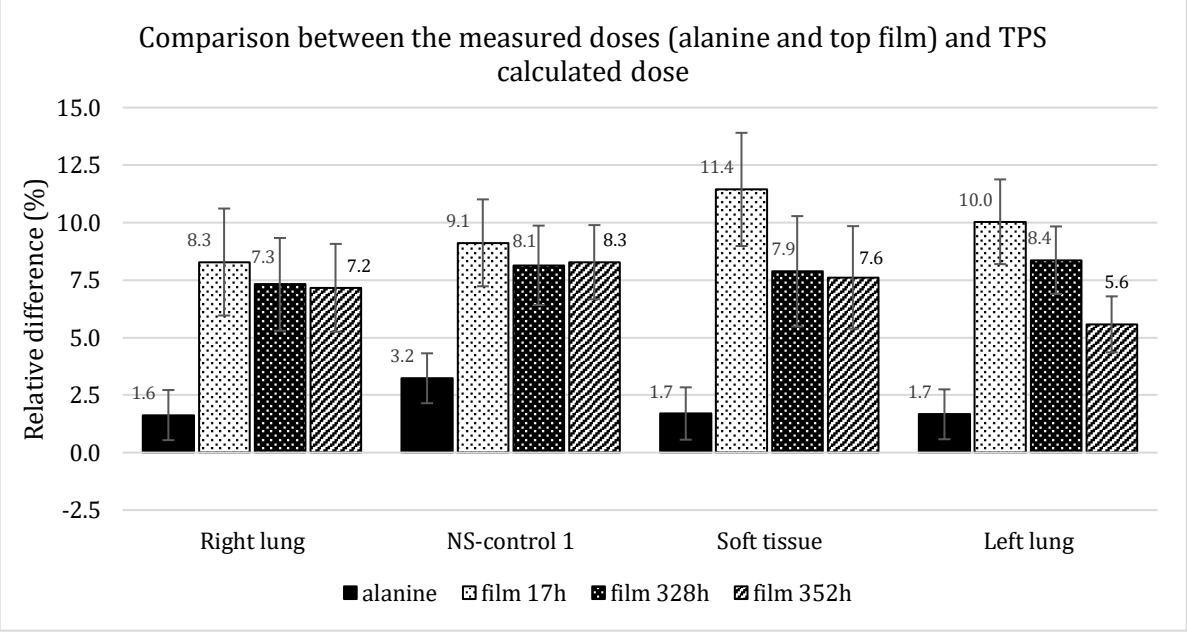

Figure 44: Dose comparison between the alanine measurement, the 3 read-outs of the top EBT3 film (after 17h, 328h and 352h) and the TPS calculations

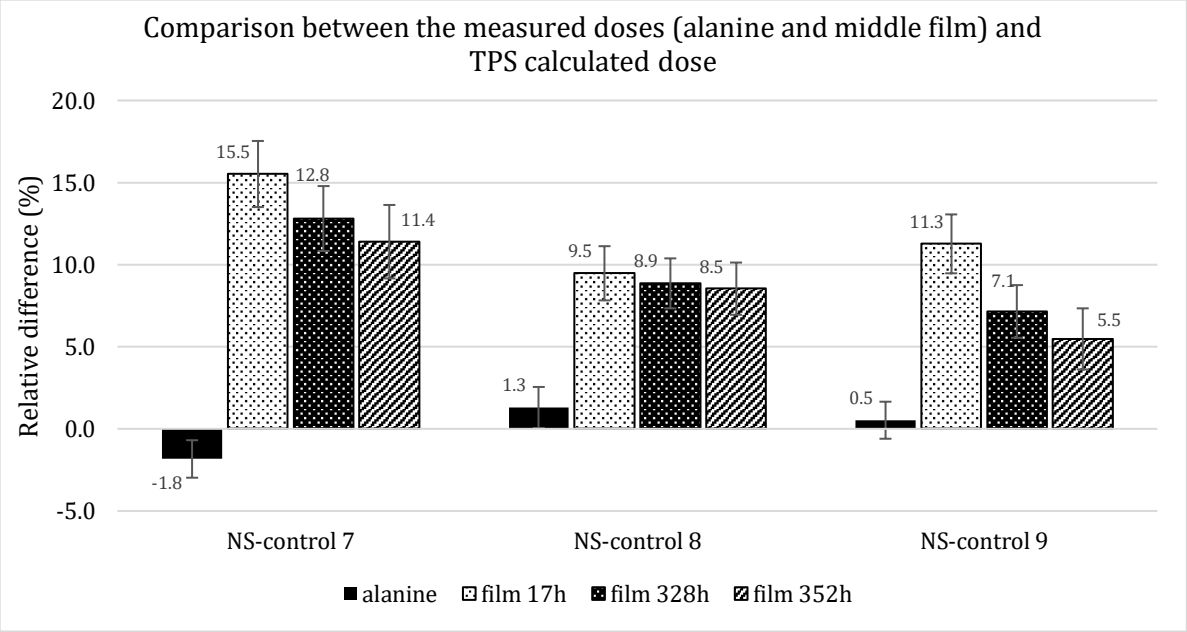

Figure 45: Dose comparison between the alanine measurement, the 3 read-outs of the middle EBT3 film (after 17h, 328h and 352h) and the TPS calculations

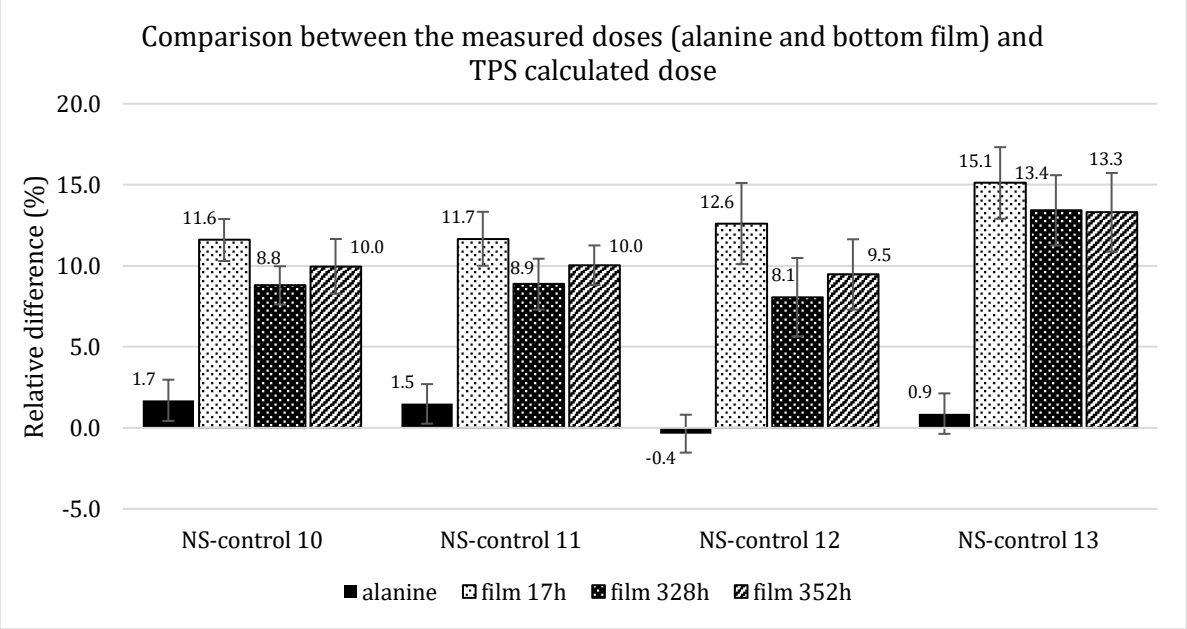

Figure 46: Dose comparison between the alanine measurement, the 3 read-outs of the bottom EBT3 film (after 17h, 328h and 352h) and the TPS calculations

4.5 Dosimetry verification of thoracic phantom clinic 2

4.5.1 One-scan calibration

Figure 47 represents the irradiated top film from inside the phantom (5 by 8 cm2 field) scanned at the same instant as the reference film irradiated with 6 Gy and the reference film irradiated with 0 Gy (not irradiated). The four alanine pellets irradiated at the same time as the reference film were read out and this value was used as the calibration value for the irradiated reference film. Via the FilmQA pro software the reference values were set to these values to rescale the pre-existing calibration curve. This was done separately for all three films in the phantom.

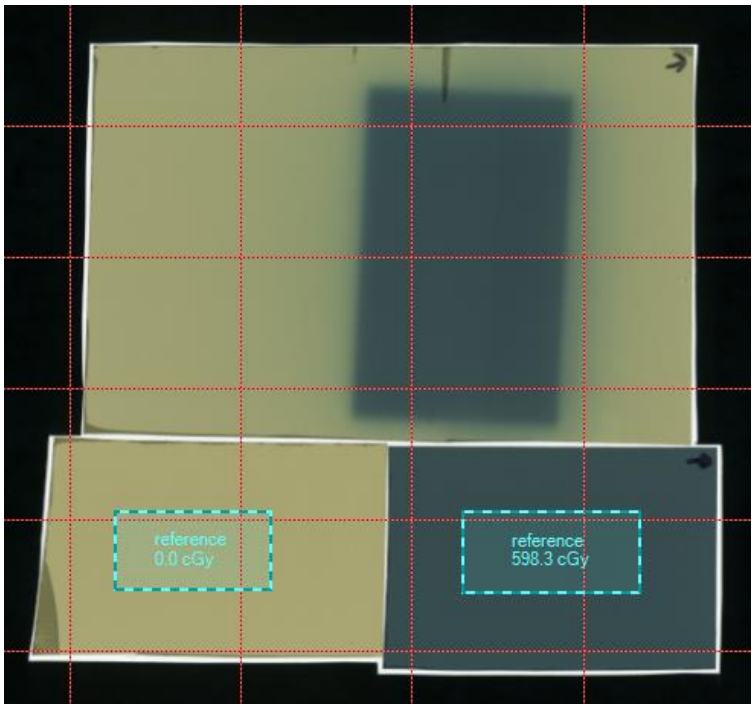

Figure 47: Top film scanned simultaneously with the two reference films of 6 and 0 Gy in order to rescale the calibration curve

4.5.2 Film dose readout

Figure 48 displays the dose profiles for the calculated dose plan by the TPS using AXBM compared to the film dose of the film located at the top position in the phantom and through the lungs while only one lung is irradiated. No significant dose differences can be noticed, which means a good accordance between the dose to the film and the calculated dose is achieved. A slightly higher dose for the lungs is present starting at 45 mm and ending at the edge of the irradiation field.

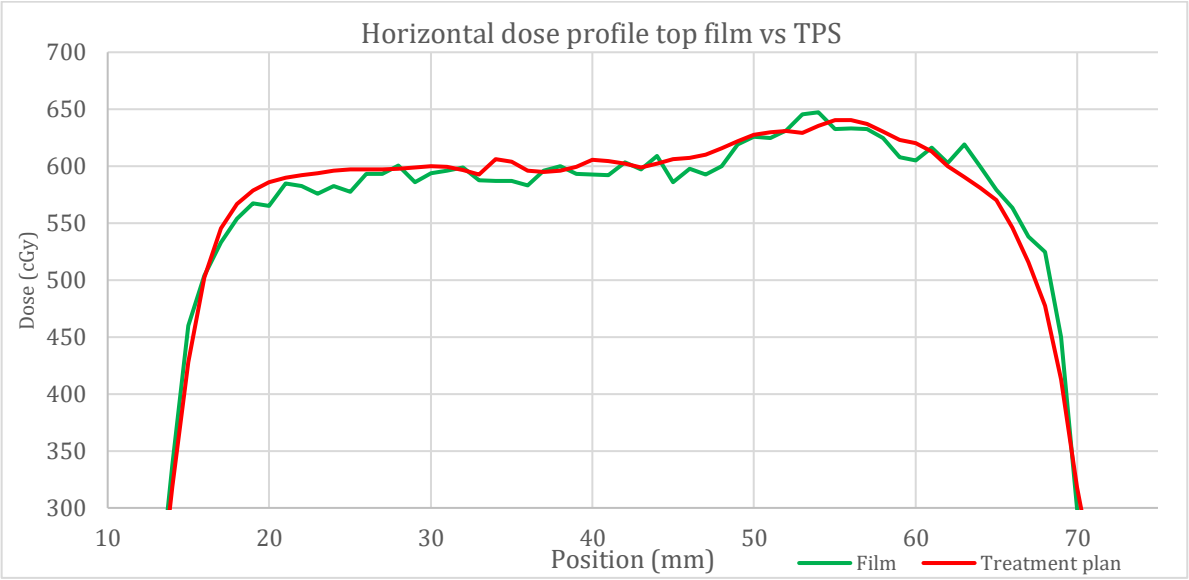

Figure 48: Horizontal dose profile comparison for the dose calculated by the TPS (AXB_M) and the measured top film dose according to the single scan calibration

Figure 49 represents the horizontal dose profiles for the calculated dose plan by the TPS using AXB_M compared to the film dose of the film located at the middle position in the phantom at the position where the lung tissue transitions to bone tissue (ribs). The film dose profile shows a distinct cutoff at approximate 75 mm due to a larger field then the film size. A higher dose for the lungs is present starting at 35 mm and ending at the edge of the irradiation field. This same region shows a mean dose underestimation by the TPS of 1.78 %. The region neighboring the lungs (only soft tissue) depicts a good correspondence for the measured dose to the calculated dose with a mean difference of 0.90 %.

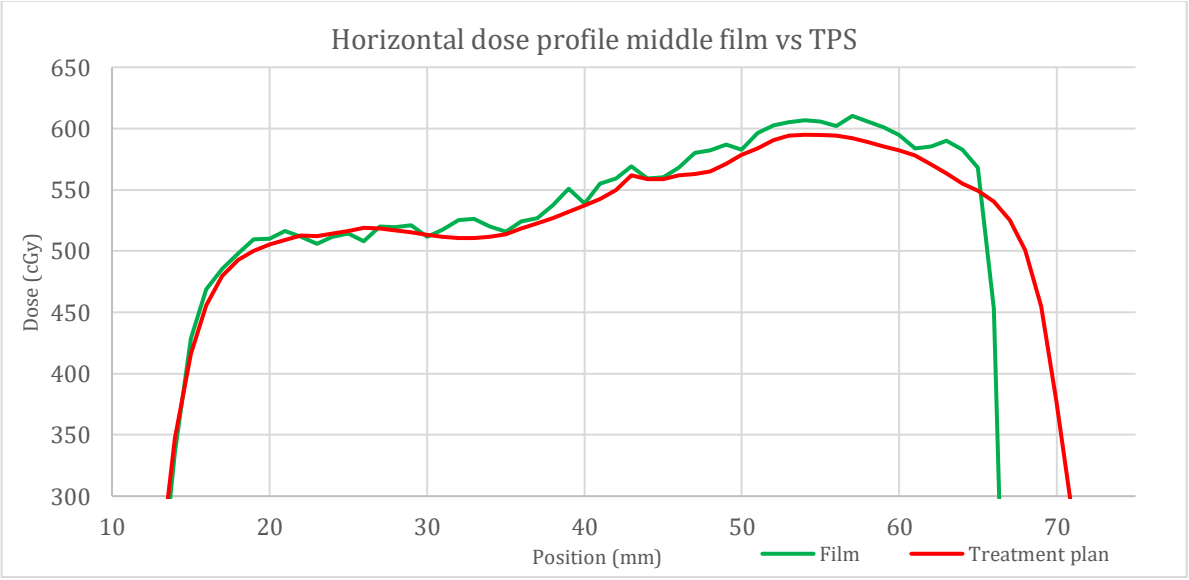

Figure 49: Horizontal dose profile comparison for the dose calculated by the TPS (AXB_M) and the measured middle film dose according to the single scan calibration

Figure 50 depicts the middle film at the same transitioning position from lung to bone/soft tissue with the vertical dose profile. The four and a half ribs can be identified by the drops in dose clearly visible for the film and the TPS although this is less significant for the lather. A significant underestimation by the TPS for the soft tissue between the ribs is noticeable. A mean underestimation for this particular area of 4.08 % is present with a max dose difference of 7.01 %.

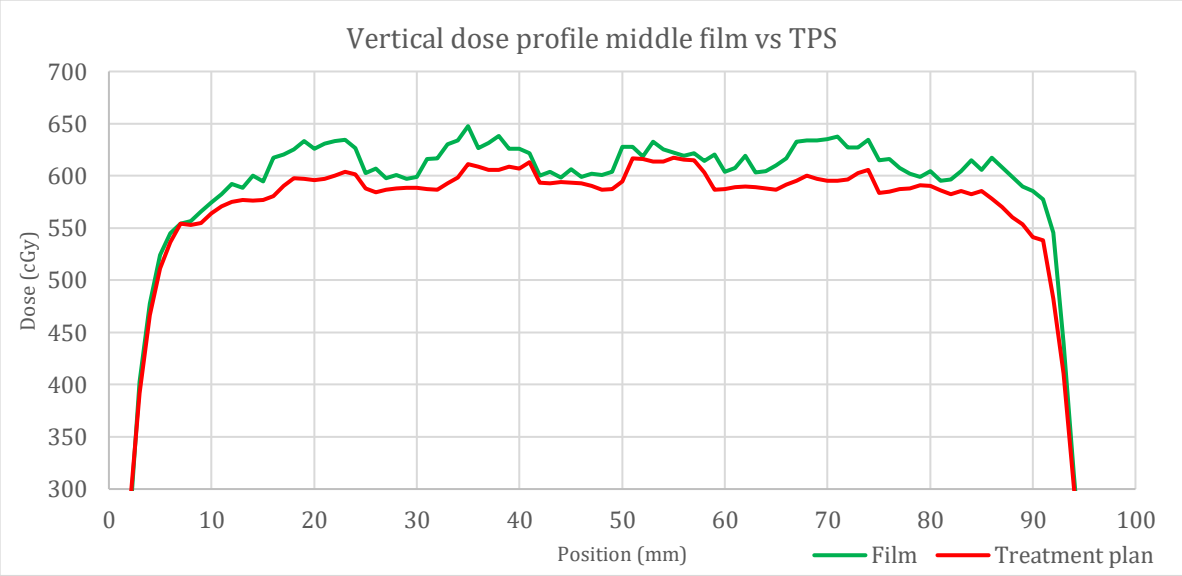

Figure 50: Vertical dose profile comparison for the dose calculated by the TPS (AXB$_M$) and the measured middle film dose according to the single scan calibration at the transition region from lung tissue to bone/soft tissue

Figure 51 displays the dose profiles for the calculated dose plan by the TPS using AXB$_M$ compared to the film dose of the film located at the bottom position in the phantom through the spine and at the position where the ribs have ended. Both curves show a good accordance to each other, especially at the position behind the lung, ribs and soft tissue. From approximately 10 to 20 mm the films is placed through the spine. The spine in front of the film has a lower density than the spine tissue behind the film. This causes a transition region from less dens to higher dens bone material. An underestimation of the dose by the TPS and a mean and max dose difference of respectively 3.65 % and 5.46 % can be noted.

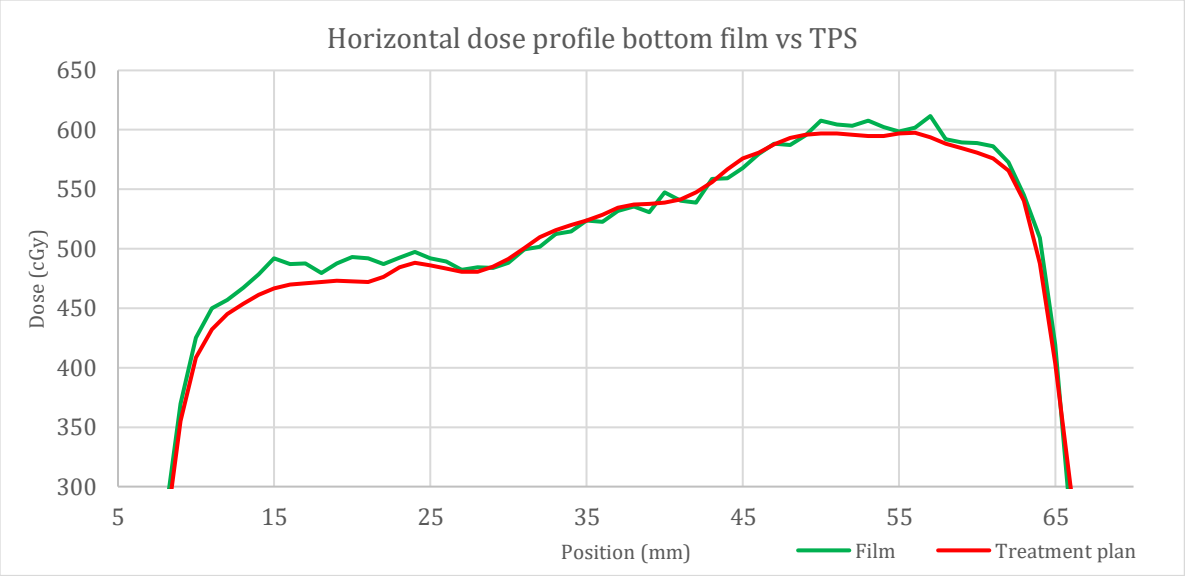

Figure 51: Horizontal dose profile comparison for the dose calculated by the TPS (AXB_M) and the measured bottom film dose according to the single scan calibration

Figure 52 depicts the bottom film with the vertical dose profiles at the region with nothing but soft tissue (center of phantom adjacent to the spine). A good correspondence for TPS calculated dose and the measured film dose is present. A mean absolute dose difference for this particular area of 0.08 % is present with a max dose difference of 3.80 %.

Figure 53 presents the vertical dose profile of the identical film depicting the entire spine length .A significant underestimation by the TPS is present at this transition region from low to higher dens bone equivalent material. A mean absolute dose difference for this particular area of 3.52 % is present with a max dose difference of 6.94 %. Also clearly visible are the alanine locations for both the film and the TPS dose profile. These are presented as two position of an average of 5.09 % higher dose than the adjacent absorbed doses in the spine.

Figure 54 depicts the bottom film with the vertical dose profiles at the region behind the lung, soft tissue and ribs. The ribs can be distinguished by the dips in the curve. The rises of dose adjacent to each rib location depict the soft tissue regions. A good correspondence for TPS calculated dose and the measured film dose is present with a slight underestimation by the TPS at the position from 80 to 100 mm. A mean absolute dose difference of 1.05 % is present with a max dose difference of 3.90 %.

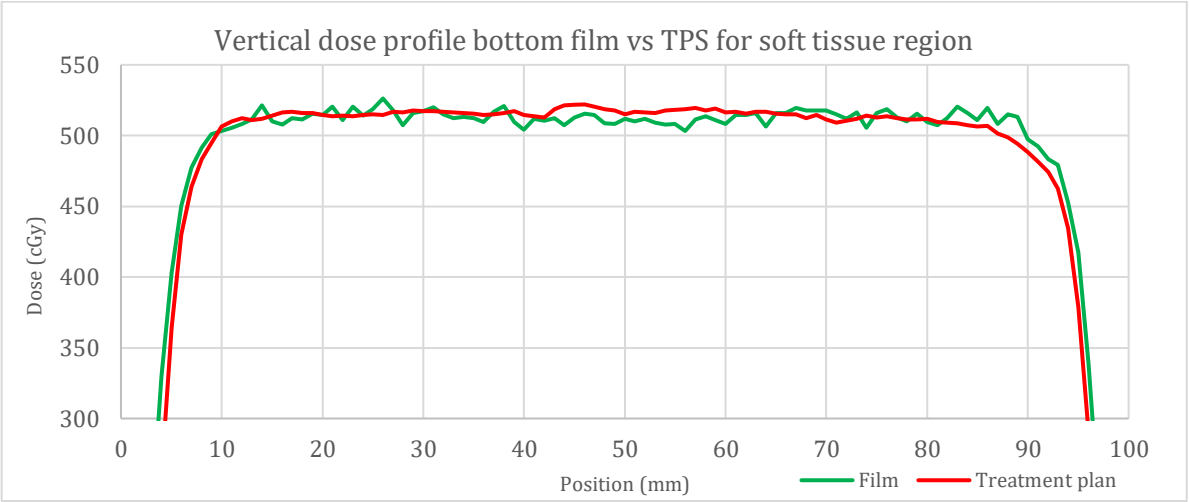

Figure 52: Vertical dose profile comparison for the dose calculated by the TPS (AXB_M) and the measured bottom film dose according to the single scan calibration at the soft tissue region

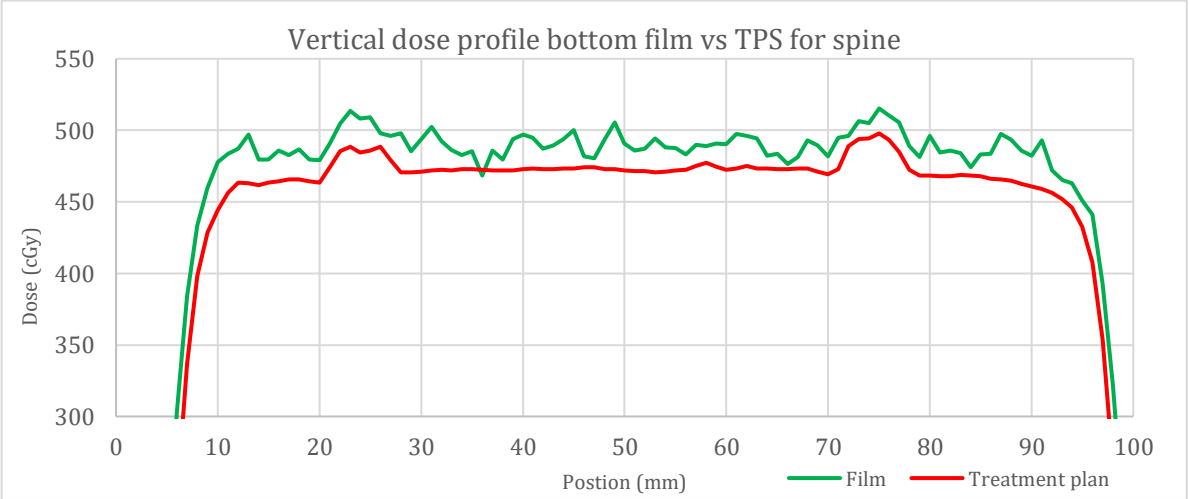

Figure 53: Vertical dose profile comparison for the dose calculated by the TPS (AXB_M) and the measured bottom film dose according to the single scan calibration at the spine region

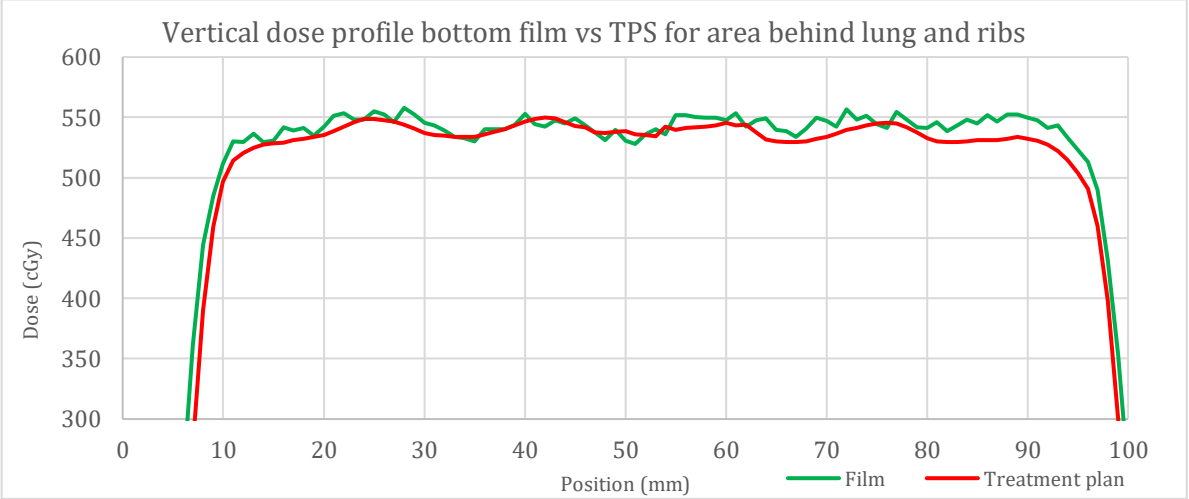

Figure 54: Vertical dose profile comparison for the dose calculated by the TPS (AXB_M) and the measured bottom film dose according to the single scan calibration at the region behind the lungs to bone/soft tissue transition

Figure 55 presents the comparison between the vertical dose profiles calculated by the TPS with a calculation grid of 2.5 mm and a calculation grid of 1.0 mm at the middle film location in the phantom. It shows that using a larger calculation grid averages out the data, thus depicting less sharp peaks.

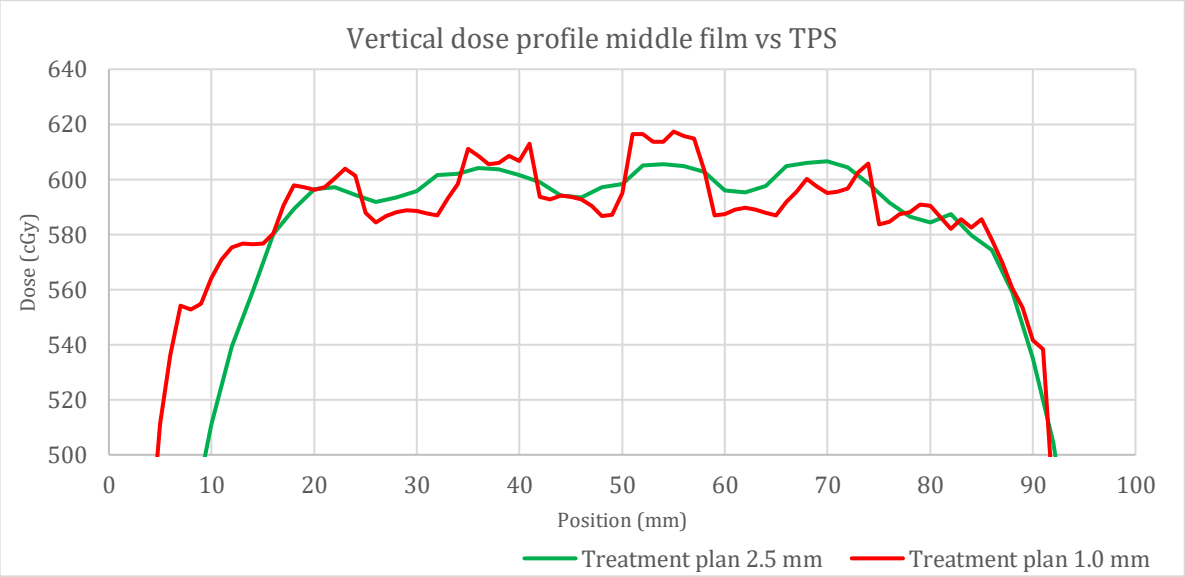

Figure 55: Comparison between vertical dose profile calculated by TPS using 2.5 mm calculation grid to 1.0 mm calculation grid

1.1.1 Alanine

Fourteen alanine pellets were fitted inside the phantom to measure the dose alongside the gafchromic EBT3 film. NS-control, NS-control 1 and 5 were located in the lungs touching the top film, NS-control 10 and 11 were located in the front part of the spine equivalent material. The rest of the pellets were found in the soft tissue equivalent material. Since a smaller field of 5 cm by 8 cm was utilized NS-control 2, 3, 5, 6, 9 and 12 should not receive a significant dose.

The results depicted in Table 12 and Figure 56 show that the relative difference between the absorbed dose calculated by the TPS using AXB_M and the measured dose does not exceed 3.08 percent with exceptions of NS-control 2, 3, 5, 6, 9 and 12 located outside the irradiation field. With such low doses for alanine, the uncertainty of the pellets located outside the irradiation field depict values conforming to the dose differences compared to the TPS for pellets 5,9 and 12. Pellets 2,3 and 6 depict differences that are unacceptably larger than the uncertainty limits.

Table 12: The mean absorbed dose calculated by the TPS, compared to the mean measured dose of the alanine with the absolute and relative difference and the location of the alanine pellets related to the film regions

		Absorbed dose				
Film region	Alanine pellet	TPS (Gy)	measured (Gy)	Absolute difference (Gy)	Relative difference (%)	uncertainty (%)
Top film	NS-control	6.298	6.467	0.169	2.68	1.09
	NS-control 1	6.275	6.469	0.193	3.08	1.09
	NS-control 2	0.107	0.200	0.093	86.45	25.06
	NS-control 3	0.109	0.180	0.071	65.39	27.73
	NS-control 4	5.715	5.854	0.139	2.43	1.15
	NS-control 5	0.140	0.178	0.038	27.47	28.01
	NS-control 6	0.041	0.124	0.083	202.25	40.33
Middle film	NS-control 7	5.898	6.047	0.148	2.51	1.13
	NS-control 8	5.009	4.944	-0.065	-1.30	1.27
	NS-control 9	0.181	0.217	0.036	19.99	23.02
Bottom film	NS-control 10	4.690	4.785	0.094	2.01	1.29
	NS-control 11	4.734	4.813	0.079	1.67	1.29
	NS-control 12	0.159	0.138	-0.021	-13.07	36.16
	NS-control 13	4.698	4.590	-0.108	-2.29	1.33

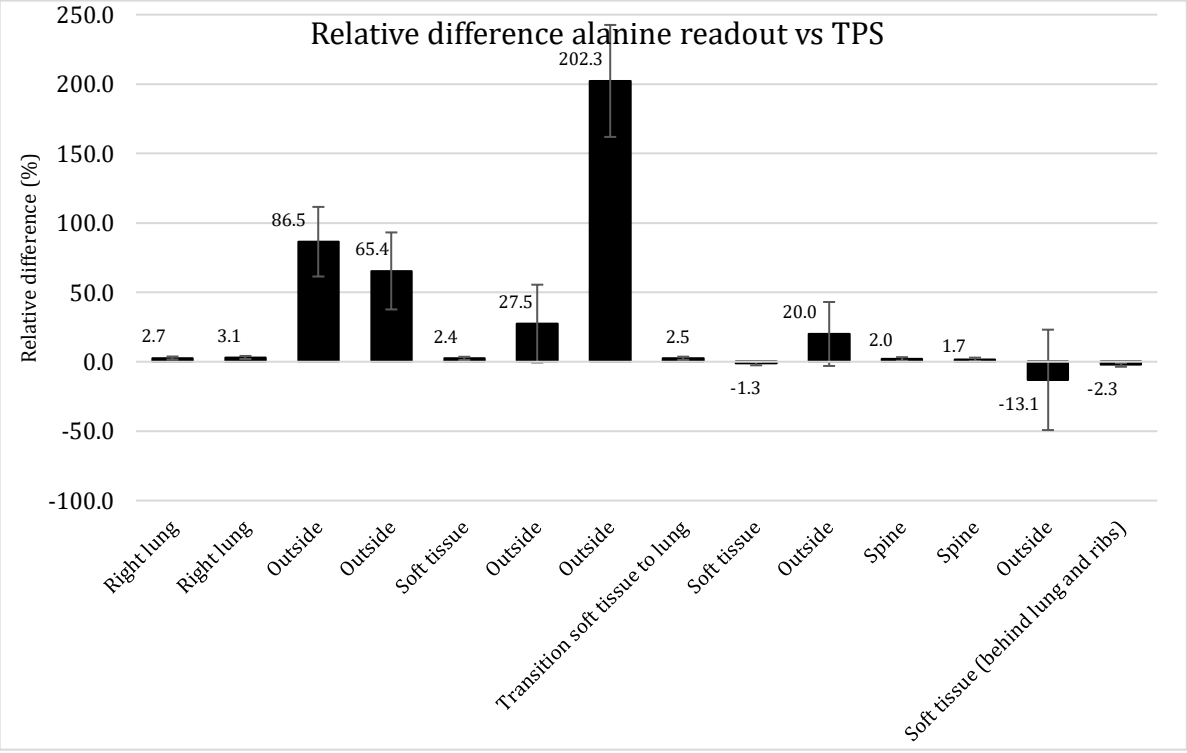

Figure 56: Relative difference between the alanine measurement and the dose calculated by the TPS for all alanine pellets: NS-control to NS-control 13

1.1.2 Total dose results comparison

Figure 57 depicts the comparison of the dose of the alanine pellets for all film regions in the phantom with the exception of the pellets placed outside of the irradiation field (NS-control 2, 3, 5, 6, 9 and 12) and the respective films to the dose calculated by the TPS using AXB_M. The alanine pellets show an acceptable deviation with a max difference of 3.1 % in the lower region of the lungs. Regarding the film at the top position, an acceptable difference of maximum -2.04 % is visible at the same location of the most significant difference of the alanine. The film however, underestimates the dose while the alanine overestimates the dose calculated by the TPS. It can be noticed that all dose measurements of the top film depict an underestimation by the film compared to the TPS, This is also the only film location presenting underestimations by the film.

At the middle film region (transition from lungs to ribs and soft tissue) in the phantom, the alanine pellets show an acceptable deviation. For pellet 8 an overestimation of the dose by the film is noticeable while the alanine depicts an underestimation compared to the dose calculated by the TPS. The maximum difference measured by the film is 3.88 % close to the spine embedded in soft tissue.

At the bottom film region (through the spine and behind the right lung) in the phantom, the alanine pellets show an acceptable deviation with a max difference of -2.3 % for pellet 13. On that same position on the film, there is an overestimation of 3.14 %. On the region of alanine pellet 10 and 11 (located in the spine) there is a good accordance alanine to the dose calculated by the TPS while the film measured doses depict a significant overestimation of 4.77 % and 4.39 %. The locations at which the alanine has an underestimation of the dose (pellet 8 and 13) is in all cases in soft tissue close to the spine.

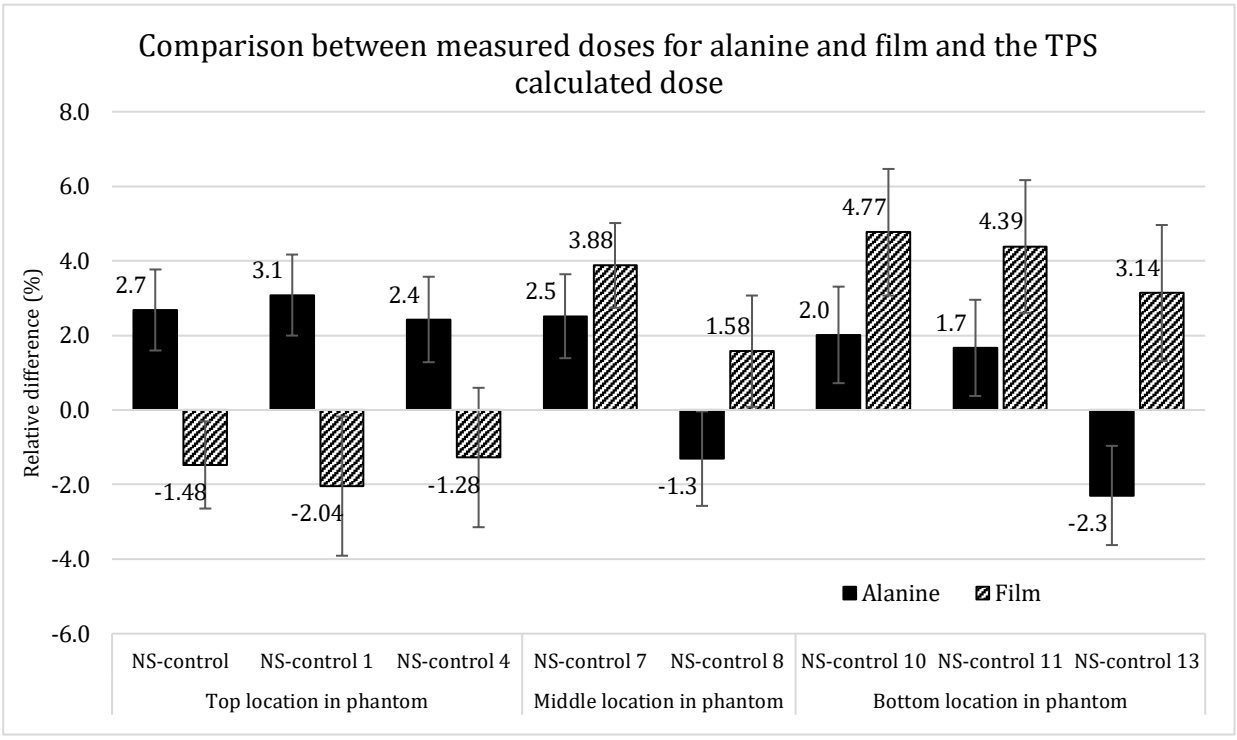

Figure 57: Dose comparison between the alanine measurement, the EBT3 film measurements and the TPS calculations

2 Discussion

2.1 3D-design and printing

During the design process for the 3D-printable thoracic phantom using Autodesk Fusion 360 it became clear that a decent amount of time would be needed to get acquainted with the program. The first idea was to design a simple phantom using only cylindrical or circular shapes. Since a phantom representable to a real human body was desired this was rapidly dismissed as more complex shapes were used for the development of the lungs and ribs. While designing the ribs, attention to the design of the molds was necessary because of the curing process of the silicone.

Since the phantom had to be cut into several different segments for placing of EBT3 films and alanine dosimeters, certain design parameters had to be altered especially for the rib cutouts and the diameter of the spine. The phantom was first designed in one complete piece and afterwards cut into 4 segments not including the lungs. Since the lungs were designed using the same dimension parameters as the insertions in the soft tissue phantom and no adjustments were performed to other segments, some fitting problems occurred after printing. Even after a serious amount of sanding the lungs were too large to fit perfect in the phantom, which caused a gap on the sides on the phantom. This, in turn, caused a non-homogenous soft tissue area in the phantom. These areas were consequently left out of the irradiation field. A solution for this would be to design and print the lungs on a scale of approximately 98 % of the original size.

Protrusions to fit each segment into the next were provided in order to have no movement of the segment while irradiating. The slope added to the top ones provided stability during printing. Since this was not added to the rib inserts, quite some PLA residue filled these inserts. It was not simple to remove these residues to be able to fit the ribs snugly.

The first design allowed the placement of alanine pellets in the ribs themselves in order to measure the accuracy for dose distribution at the transition area from lung tissue to bone tissue. Due to the dimension limitations of the 3D-printer and the extra complication of having to use some sort of adhesion chemical in order to complete the original sized phantom, it was opted to scale the entire phantom to 75 % of its original dimensions. Consequently, the ribs decreased in size and were not large enough anymore to fit an entire alanine pellet.
It was decided to fit alanine pellets in the spine by adding protrusions to the lid of the spine mold and having the front of the spine containing less $CaCO_3$ than the back in order to create a transition area of low dens (same density as the ribs) to higher dens bone material. This mold design was accompanied with holes in the lid to extract excess silicone which worked as a charm.

2.2 Choice of bone equivalent material

The first silicone that was tested was Bluesil RTV-141 named as silicone type 1 and showed terrible homogeneity of the $CaCO_3$ on the CT-scan since the curing process took too long, causing the $CaCO_3$ to settle on the bottom of each sample. Adding heat would drop this time but it was not certain that this would suffice and an oven would be necessary and was not always available. Furthermore, PLA starts melting at a temperature of approximately 170 °C offering relative low heat resistance for the molds. A second type of RTV silicone (ZA 00 Translucid) was soon after investigated and proved a much greater homogeneity after a relative short curing time at room temperature of approximately 1 hour. One disadvantage of this rapid curing time occurred which was the presence of air pockets throughout the samples. Tapping or adding other forms of vibration to the mixing container and the fact that the ribs and the two parts of the spine had a relatively small thickness ensured a low amount of air inside the cured silicone.

Regarding Figure 32 the relevant values and curve proved to be the one depicting the maximum HU in relation to the amount of $CaCO_3$ added due to the fact that the other two curves are influenced by the air pockets in the samples and consequently in the regions of interest. To achieve CT-values conforming to real rib and low dens spine tissue 3 grams of $CaCO_3$ can to be added to 10 milliliters RTV silicone and 5 grams achieves higher CT-values conforming to the denser spine tissue. When using 3 grams a mass density of 1.23 g/ml is achieved which is 0.105 g/ml lower than the value calculated by the TPS using a mean CT-value of 425 HU. Because of this a higher RED is used for calculation of the dose distribution. A RED of 1.25 - 1.30 should correspond to 425 HU as is also calculated by the TPS (RED TPS = 1.28). Since the mass density of 1.23 g/ml is lower for the bone equivalent material a RED corresponding to approximately 425 HU should be in the range of 1.14 – 1.20. Consequently these would be the values needed for correct calculation of the dose distribution. Calcium phosphate ($Ca_3(PO_4)_2$) could offer a better representation to human bone tissue due to the higher density of 3.14 g/ml resembling a higher relative electron density compared to $CaCO_3$ having a density of 2.71 g/cm^3 provided it has an equal or better solubility.

2.3 Imaging properties

Variations in infill density were measured in several segments of the 3D-printed phantom. Two segments showed a variation of infill density when comparing the left to the right side. This is most probably caused by some sort of irregularity during the printing process, such as changing the PLA coil during the printing process of the segment.
However this did not result in issues regarding the dosimetry since a normal human body is heterogenous of nature and the calculated density by the TPS is based on the CT-scan. If the conversion curve is correct the uniformity does not matter. It should however be taken into account when high-quality, detailed structures are needed. This added extra challenges to the dose calculation by the TPS that are also present in the day to day workflow in radiotherapy.

Figure 33 clearly visualizes the edges of all segments having a high infill to ensure a certain strength to the structure. This offers no real consequences for the soft tissue segments since these have an infill density of 90 %. However for the lungs this does have consequences at the region where the lungs are separated. This can be avoided by either separating the lungs after 3D-printing, adding new difficulties, or by printing them without a border on the interior side.

All bone structures show CT-values comparable to real ribs and spine. All four segments of the lungs show good conformity to each other with a slightly lower mean value of Hounsfield Units than predicted which means an infill density of 35 - 40 % instead of the used 30 % may be more favorable. Every segment shows an standard deviation of more than 100. This is caused by the way of printing the infill. The infill structure can be chosen and in this case a triangular structure was opted for. Each corner has three side attachments which in turn causes a higher amount of PLA than the separate sides of the triangles. This combined with the fact that the low infill is designed using more air and less PLA gives a significant standard deviation on the CT-values since high value contrasts are present.

When considering the properties of the 3D-printed phantom using the prediction by the TPS as shown in Table 10, all materials show great results. The lungs are calculated as 100 % lung tissue, for the soft tissue , variations are presented since different densities are present. The best case is predicted as 24 % adipose tissue and 76 % skeletal muscle and offered CT-values of -36 HU having a mass density of 0.993 g/cm^3 and relative electron density of 0.983 resembling values for water and thus soft tissue. The worst case was predicted as 100 % adipose tissue with a mass density of 0.908 g/cm^3 and a relative electron density of 933 which is certainly not a bad representation but is quite a large deviation from the desired values.

When considering the properties of the bone equivalent material using the prediction by the TPS, the material shows great results. The ribs and front part of the spine are predicted as 53 – 54 % cartilage with 47 – 48 % bone tissue. This high amount of cartilage is not desired since this is not present in human ribs and is caused by the relative low mass density and CT-values when trying to mimic human ribs.

For the denser back part of the spine 30 % cartilage an 70 % bone is predicted by the TPS giving more equivalent values. This would mean that mimicking denser human bone tissue using ZA 00 Translucid would have greater equivalent values as long as the silicone does not reach its saturation level.

2.4 Dosimetric properties

2.4.1 Clinic 1

Using the standard calibration using a pre-defined calibration curve resulted in significant differences in dose between the TPS calculated dose using the dose to medium calculation algorithm and the EBT3 film dose. In all cases and all films an overdosage seemed to happen. This can be caused by the fact that it was not certain that the calibration curve was set up using the same batch of films. This dose difference is presumed to not have been caused by an underestimation of the TPS calculation algorithm.

Due to the uncertainty on the read outs of the films combined with the relative large calculation grid of 2.5 mm, any effects of the bone equivalent material cannot be distinguished. When viewing the TPS curves depicting the top film region, it shows a higher dose in the lungs, then lowering while reaching its lowest point at the edge of the lungs and adjacent to the edge of the middle soft tissue while rising slightly at the center of this soft tissue segment. This would be caused by the high density edges of the 3D-printed segments. Only the general curve shape of the film dose profile is similar to the TPS curve with no distinguishing of the subtle details visible. The same is noticeable with the curves the bottom film position (Figure 39). The TPS shows the lower dose at the spine region and higher dose at the lung region depicting an almost symmetrical curve. The film dose profile presents no significant dose variation at the spine region and a lower dose at one half of the right lung compared to the left region. This is the part where more soft tissue precedes the lung.

Furthermore concerning the middle film position it was significantly more difficult to get a good alignment of the film to the dose map using FilmQA Pro since the irradiation field of 10 cm by 10 cm was larger than the dimension of the film at this position of the phantom. However comparing the dose profiles of the lung region and the soft tissue region at this depth in the phantom a more significant overdosage for the lungs is present. This can be due to the transition from lung tissue to bone and soft tissue at this particular region.

The alanine dosimetry showed a good conformity between the TPS calculated dose and the measured dose with 1 pellet inside the actual irradiation field showing an underestimation by the TPS of 3.23 %. Disregarding this one pellet the maximum difference amounts to -1.84 %, taking into account the uncertainty for the alanine, this amounts to a value sufficiently lower than 2 %. For the alanine pellets located inside the spine equivalent material an underestimation of only 1.70 and 1.48 % is made by the TPS. This would mean a good accordance for alanine and the TPS and since this is the more reliable method of medical dosimetry for doses ranging from 5 to 25 Gy, the absolute results achieved by the film dosimetry should be disregarded.

2.4.2 Clinic 2

Using the one-scan calibration method a good accordance between all horizontal dose profiles is noticeable at following transition locations: soft tissue – soft tissue, lung – lung and lung – bone. At the transition area of low density bone to higher density bone depicted in Figure 51 an underestimation for the dose by the TPS of 3.65 % is present. This deviation is confirmed when looking at the vertical dose profile through the entire spine with a mean underestimation of 3.52 % meaning adaptations should be considered if not taking in account the uncertainty of 1.58 %.

A similar effect can be noticed on the vertical dose profile for the middle film location perpendicular to the ribs. A significant underestimation by the TPS having an average value of 4.08 % in presented for the parts where transitioning from lung to soft tissue in between bone equivalent material occurs. The transitioning from lung tissue to bone equivalent material depict a significant lower deviation of 1.78 % average. It can be stated that only transition areas containing or neighboring bone equivalent tissue deliver calculation issues for the TPS since both the horizontal and vertical dose profiles at the lowest location in the phantom underneath lung and ribs presents a good accordance for calculated and measured dose. The underestimation is most likely caused because of less attenuation occurring than predicted by the TPS due to a lower mass-density than human bone for the similar CT-values.

The alanine dosimetry presented a good conformity between the TPS calculated dose and the measured dose with 1 pellet inside the actual irradiation field showing an underestimation by the TPS of 3.1 %. Disregarding this one pellet the maximum difference amounts to 2.7 %, taking into account the uncertainty for the alanine, this amounts to a value lower than 2 %. For the alanine pellets located inside the spine equivalent material an underestimation of only 2.0 % and 1.7 % is made by the TPS. Interestingly an overestimation is made by the TPS for the locations very close but not in the spine according to the alanine. The values of these underestimations are -1.3 % at the middle film location and -2.3 % at the lowest film location. These are the only instances where an overestimation by the TPS in comparison to the alanine occurs.

Concerning the calculation grid of the TPS it can be stated that using the grid of 1.0 mm, a higher resolution of the dose profile can be achieved. This dose profile depicts a better accordance to the resolution and dose profile of the measured dose by the film in comparison to the results of the 2.5 mm grid. This was caused due to the fact that the ribs and soft tissue between them are only about 7 mm in width. Because of this, the results are averaged out over the distance of 2.5 mm between each measurement point by the TPS causing a slight overestimation for lower doses (bone equivalent tissue) and a slight underestimation for higher doses (soft tissue). Overall if a smaller grid is chosen, calculation of the results will take longer with isodoses more closely following density changes. It has to be taken into account that memory problems can occur if the grid is too small.

However a smaller grid size should be implemented for stereotactic radiotherapy or other cases where higher resolution is required since the grid size only influences the accuracy and resolution bot not the dose delivery if the monitoring units are kept identical.

2.4.3 Comparison clinic 1 to clinic 2

The comparison for the EBT3 film dosimetry will not be performed since the calibration curve used for the processing of the read out of the films in clinic 1 was recalibrated using the one-scan method in clinic 2. Consequently a comparison between these results does not add any additional value. For the alanine dosimetry however it can be noted that for the top film region a similar response is present between clinic 1 and 2, with the maximum dose difference to the TPS having a value of 3.2 % for clinic 1 and 3.1 % for clinic 2 at the same location in the right lung. These dose differences can be caused because of the fact that the preceding lung segment has a low density but the edge where the lung is separated and the alanine is placed has a higher density causing difficulties in dose calculation at this transition point.

For the middle film location an underestimation by the TPS in comparison to the alanine is presented for NS-control 7 (between ribs) at clinic 2 and for NS-control 8 (next to spine) at clinic 1, while an overestimation by the TPS is made for pellet 7 at clinic 1 an pellet 8 at clinic 2. Since these locations are both transition or very close to transition areas, the cause of this has a high probability of being dose calculation errors due to the theoretical and practical density variations. For the lowest location in the phantom only pellet 13 presents a high variation on dose difference between clinic 1 and 2, These results however, are in line with the variations seen between the two clinics for pellet 8. Which should be logical since they are positioned at the same lateral distance from the center of the phantom at a different depth.

3 Conclusion

The aim of this Master's thesis and in particular the practical study was to investigate the possibility to create a 3D-printed thoracic phantom containing bone equivalent material that can be produced cheaply and easily while providing imaging and dosimetry properties that are up to standard for dosimetry in radiotherapy. Firstly a thoracic phantom was designed and 3D-printed providing room for ribs and a spine.
Secondly, a rib equivalent material was investigated using two types of RTV-silicone mixed with various amounts of $CaCO_3$. ZA 00 Translucid proved to have ideal properties and an acceptable curing time to create a homogenous mixture to serve as bone equivalent material.

Next the imaging properties were investigated of all 3D-printed materials (soft tissue and lung) and the bone equivalent material. All four segments of the lungs offered good CT-values corresponding to human lungs of around -770 HU at 30 % infill density. The soft tissue segments showed variations in CT-values ranging from -58.32 to -132.45 HU when 0 HU was desired at 90 % infill density. The bone equivalent material presented CT-values of 482.72 HU for lower density bone and 695.42 HU for higher density bone which were both within the predicted range. The mass density of the bone equivalent material of 1.23 g/ml for the lower density bone (ribs) would be preferred higher at the same CT-values.

Lastly, dosimetry was performed using a combination of EBT3 gafchromic films and L-α-alanine in two separate clinics. The results showed that using the single scan method provides an accurate method for dose measurements in comparison to the standard calibration method for EBT3 film dosimetry utilizing FilmQA Pro. The dose calculated with the Acuros dose to medium algorithm was in accordance to the measured dose of the films and the alanine. Only transition areas involving the bone equivalent material presented underestimations by the TPS by up to 4.08 % for the EBT3 film when transitioning from lung tissue to soft tissue adjacent to the bone equivalent material. These transition areas containing the bone equivalent material also offered some calculation difficulties when looking at the alanine dosimetry. They show an underestimation by the TPS for one pellet at clinic 1 while the same pellet depicted an overestimation in clinic 2. The overall max deviations were 3.2 % for clinic 1 and 3.1 % for clinic 2 at the same location in the right lung, giving good conformity in this aspect.

Future adaptations should be considered when attempting to fabricate a radiotherapeutic dosimetry phantom. All inner fitting segments should be scaled in order to fit perfectly into each other while removing the edges of every segment especially for the lungs. A high-quality 3D-printer is certainly advised when desiring accurate and detailed results. Furthermore, a denser substitute to $CaCO_3$ like $Ca_3(PO_4)_2$ in combination with rapidly curing RTV-silicone is advised in order to achieve representable dosimetry and imaging results.

Bibliography

[1] F. Viel, “Developing Quality Assurance Procedures for Gated Volumetric Modulated Arc Therapy in Stereotactic Ablative Radiation Therapy,” no. March, 2014.

[2] R. Baskar, K. A. Lee, R. Yeo, and K. W. Yeoh, “Cancer and radiation therapy: Current advances and future directions,” *Int. J. Med. Sci.*, vol. 9, no. 3, pp. 193–199, 2012.

[3] S. P. Frigo, “Radiation therapy dosimetry phantoms,” in *The Phantoms of Medical and Health Physics*, 2013, pp. 17–38.

[4] TOMSK POLYTECHNIC UNIVERSITY, “Advanced dosimetry phantoms improving radiotherapy verification,” *EurekAlert*, 2018. [Online]. Available: https://www.eurekalert.org/pub_releases/2018-02/tpu-adp020118.php.

[5] A. Fogliata, G. Nicolini, A. Clivio, E. Vanetti, and L. Cozzi, “Dosimetric evaluation of Acuros XB Advanced Dose Calculation algorithm in heterogeneous media,” *Radiat. Oncol.*, vol. 6, no. 82, pp. 1–15, 2011.

[6] J. F. Winslow, D. E. Hyer, R. F. Fisher, C. J. Tien, and D. E. Hintenlang, “Construction of anthropomorphic phantoms for use in dosimetry studies,” *J. Appl. Clin. Med. Phys.*, vol. 10, no. 3, pp. 195–204, 2009.

[7] F. Adams *et al.*, “Soft 3D-Printed Phantom of the Human Kidney with Collecting System,” *Ann. Biomed. Eng.*, vol. 45, no. 4, pp. 963–972, 2017.

[8] F. Zhang *et al.*, “Design and fabrication of a personalized anthropomorphic phantom using 3D printing and tissue equivalent materials,” *Quant. Imaging Med. Surg.*, vol. 9, no. 1, pp. 94–100, 2019.

[9] T. Kairn, S. B. Crowe, and T. Markwell, “Use of 3D Printed Materials as Tissue-Equivalent Phantoms,” *IFMBE Proc.*, vol. 51, pp. 3–7, 2015.

[10] E. D. Ehler, B. M. Barney, P. D. Higgins, and K. E. Dusenbery, “Patient specific 3D printed phantom for IMRT quality assurance,” *Phys. Med. Biol.*, vol. 59, no. 19, p. 5763, 2014.

[11] S. J. Howlett, “Monitor unit calculation for tangential breast treatments: Verification in an anthropomorphic phantom,” *J. Appl. Clin. Med. Phys.*, vol. 3, no. 3, p. 235, 2002.

[12] T. Holmes, C. Ma, and L. Wang, “Monitor Unit,” *Encycl. Radiat. Oncol.*, vol. 1, no. 1, 2013.

[13] F. Nordström, *Quality Assurance in Radiotherapy - Development and evaluation of new tools for improved patient safety*. 2012.

[14] M. Nakao *et al.*, “Tolerance levels of mass density for CT number calibration in photon radiation therapy,” *J. Appl. Clin. Med. Phys.*, vol. 20, no. 6, pp. 45–52, 2019.

[15] L. Dhamers, J. Withouck, K. Bamps, K. Tournel, and B. Reniers, “Implications with the implementation of Acuros : a comparison between AAA and Acuros on dose calculations.”

[16] D. Burns *et al.*, “Calibration of Reference Dosimeters for External Beam Radiotherapy,” *Calibration Ref. Dosimeters Extern. Beam Radiother.*, no. 469, 2009.

[17] J. V Siebers, P. J. Keall, and E. Alan, “Converting absorbed dose to medium to absorbed dose to water for Monte Carlo based photon beam dose calculations,” *Phys. Med. Biol.*, vol. 45, no. 983, p. 14, 2000.

[18] T. Knoos and B. Mcclean, “Dose calculation algorithms in algorithms in 3DCRT and IMRT,” *Med. Phys.*, vol. 35, no. 6, p. 2930, 2008.

[19] S. Park, J. M. Park, C. H. Choi, M. Chun, and J. Kim, “Dosimetric Validation of the Acuros XB Advanced Dose Calculation Algorithm for Volumetric Modulated Arc Therapy Plans,” vol. 27, no. 4, pp. 180–188, 2016.

[20] L. Dhamers, B. Reniers, and K. Tournel, “Dose verification in lung SBRT and implications with the clinical implementation of Acuros,” p. 66, 2019.

[21] Wiener Krankenanstaltenverbund, “Dose behind Titanium.” [Online]. Available: https://www.wienkav.at/kav/kfj/91033454/physik/eclipse/AXB13.htm.

[22] O. Baffa and A. Kinoshita, “Clinical applications of alanine/electron spin resonance dosimetry,” *Radiat. Environ. Biophys.*, vol. 53, no. 2, pp. 233–240, 2014.

[23] B. H. Østerås, E. O. Hole, D. R. Olsen, and E. Malinen, “EPR dosimetry of radiotherapy photon beams in inhomogeneous media using alanine films,” *Phys. Med. Biol.*, vol. 51, no. 24, pp. 6315–6328, 2006.

[24] B. Schaeken, C. Goor, and P. Scalliet, “143 EPR/alanine dosimetry: just another dose measuring system?,” *Eur. J. Cancer*, vol. 31, no. 6, p. S33, 1995.

[25] J. Helt-Hansen, F. Rosendal, I. M. Kofoed, and C. E. Andersen, “Medical reference dosimetry using EPR measurements of alanine: Development of an improved method for clinical dose levels,” *Acta Oncol. (Madr).*, vol. 48, no. 2, pp. 216–222, 2009.

[26] M. Anton, “Uncertainties in alanine/ESR dosimetry at the Physikalisch-Technische Bundesanstalt,” *Phys. Med. Biol.*, vol. 51, no. 21, p. 5419, 2006.

[27] M. Mathot, S. Sobczak, and M. T. Hoornaert, “Gafchromic film dosimetry: Four years experience using FilmQA Pro software and Epson flatbed scanners,” *Phys. Medica*, vol. 30, no. 8, pp. 871–877, 2014.

[28] J. Sorriaux *et al.*, “Evaluation of Gafchromic® EBT3 films characteristics in therapy photon, electron and proton beams,” *Phys. Medica*, vol. 29, no. 6, pp. 599–606, 2013.

[29] V. C. Borca *et al.*, “Dosimetric characterization and use of GAFCHROMIC EBT3 film for IMRT dose verification,” *J. Appl. Clin. Med. Phys.*, vol. 14, no. 2, pp. 158–171, 2013.

[30] “Gafchromic™ Dosimetry media, type ebt-xd.”

[31] D. Lewis, A. Micke, and X. Yu, “An efficient protocol for radiochromic film dosimetry and measurement in a single scan An efficient protocol for radiochromic film dosimetry combining,” *Med. Phys.*, vol. 39, no. 10, pp. 6339–6350, 2012.

[32] G. R. Veneziani, E. L. Corrêa, M. P. A. Potiens, and L. L. Campos, “Attenuation coefficient determination of printed ABS and PLA samples in diagnostic radiology standard beams,” *J. Phys. Conf. Ser.*, vol. 733, no. 1, 2016.

[33] C. L. Ventola, “Medical Applications for 3D Printing: Current and Projected Uses,” *P&T*, vol. 39, no. 10, pp. 704–711, 2014.

[34] International Atomic Energy Agency, “Technical reports series no. 457 Dosimetry in diagnostic radiology: An international code of practice,” 2007.

[35] C. N. Ionita *et al.*, “Challenges and limitations of patient-specific vascular phantom fabrication using 3D Polyjet printing,” *SPIE Proc.*, no. 716, 2014.

[36] R. Mayer, P. Liacouras, A. Thomas, M. Kang, L. Lin, and C. B. Simone II, “3D printer generated thorax phantom with mobile tumor for radiation dosimetry,” *Rev. Sci. Instrum.*, vol. 86, no. 7, 2015.

[37] B. A. Hamedani, A. Melvin, K. Vaheesan, S. Gadani, K. Pereira, and A. F. Hall, “Three-dimensional printing CT-derived objects with controllable radiopacity,” *J. Appl. Clin. Med. Phys.*, vol. 19, no. 2, pp. 317–328, 2018.

[38] J. Solomon, A. Ba, F. Bochud, and E. Samei, “Comparison of low-contrast detectability between two CT reconstruction algorithms using voxel-based 3D printed textured phantoms,” *Med. Phys.*, vol. 43, no. 12, pp. 6497–6506, 2016.

[39] G. Menikou, T. Dadakova, M. Pavlina, M. Bock, and C. Damianou, “MRI compatible head phantom for ultrasound surgery,” *Sci. direct*, vol. 57, pp. 144–152, 2015.

[40] L. Lhotska, L. Sukupova, I. Lackovic, and G. S. Ibbott, *World Congress on Medical Physics and Biomedical Engineering 2018*, vol. 68/2. 2018.

[41] O. L. Dancewicz, S. R. Sylvander, T. S. Markwell, S. B. Crowe, and J. V Trapp, “Radiological properties of 3D printed materials in kilovoltage and megavoltage photon beams,” *Phys. Medica*, vol. 38, pp. 111–118, 2017.

[42] A. J. Cloonan, D. Shahmirzadi, R. X. Li, B. J. Doyle, E. E. Konofagou, and T. M. McGloughlin, “3D-Printed Tissue-Mimicking Phantoms for Medical Imaging and Computational Validation Applications,” *3D Print. Addit. Manuf.*, vol. 1, no. 1, pp. 14–23, 2014.

[43] Zhermack S.P.A. hitech division, “ZA 00 TRANSLUCID : Technical Data Sheet.”

[44] F. Chambon and H. H. Winter, “Linear Viscoelasticity at the Gel Point of a Crosslinking PDMS with Imbalanced Stoichiometry,” *J. Rheol. (N. Y. N. Y).*, vol. 31, no. 8, pp. 683–697, 1987.

[45] J. Mark E., B. Erman, and F. Eirich R., *Science and technology of rubber*, vol. 53, no. 3. 2005.

[46] A. S. Akiba, M., Hashim, “Vulcanization and Crosslinking,” *Prog. Polym. Sci.*, vol. 22, no. 96, pp. 475–521, 1997.

[47] B. G. D. Andersen, “Protein , Calcium and Bone Density , Part 1,” 2019. [Online]. Available: https://www.dynamicchiropractic.com/print_friendly.php?pr_file_name=https%3A%2F%2Fwww.dynamicchiropractic.com%2Fmpacms%2Fdc%2Farticle.php%3Fid%3D15392%26no_paginate%3Dtrue%26p_friendly%3Dtrue. [Accessed: 29-Nov-2019].

[48] C. B. Saw, A. Loper, K. Komanduri, T. Combine, S. Huq, and C. Scicutella, “Determination of CT-to-density conversion relationship for image-based treatment planning systems,” *Med. Dosim.*, vol. 30, no. 3, pp. 145–148, 2005.